Title

Investigating the 18-membered macrocyclic chelator NOON-2py for the detoxification of Cd^{2+}, Hg^{2+}, and Pb^{2+}

Journal

Inorganic Chemistry Frontiers

Authors

Lieberum, Jacy R

Traylor, Jane M

Jensen, Marianne L

et al.

Publication Date

2026

DOI

10.1039/d6qi01183g

Investigating the 18-Membered Macrocyclic Chelator NOON-2py for the Detoxification of Cd^{2+}, Hg^{2+}, and Pb^{2+}

Jacy R. Lieberum,[a] Jane M. Traylor,[a] Marianne L. Jensen,[b] Stephan P.A. Sauer,[c] Lars Hemmingsen,[c] Justin J. Wilson*[a]

[a] Department of Chemistry & Biochemistry, University of California Santa Barbara, Santa Barbara, California, 93106, USA
[b] The Niels Bohr Institute, University of Copenhagen, Universitetsparken 5, 2100 København Ø, Denmark
[c] Department of Chemistry, University of Copenhagen, Universitetsparken 5, 2100 København Ø, Denmark
* Corresponding author, e-mail: justinjwilson@ucsb.edu

Abstract

Chelation therapy is the primary treatment strategy for heavy metal intoxication; however, clinically used chelators, such as ethylenediaminetetraacetic acid (EDTA), exhibit poor selectivity for toxic metals over endogenous ions like Ca^{2+} and Zn^{2+}. EDTA and related chelators are anionic at physiological pH and not cell-permeable. Here, we investigated the diaza-18-crown-6-based ligand NOON-2py (7,16-bis(pyridin-2-ylmethyl)-1,4,10,13-tetraoxa-7,16-diazacyclooctadecane) for its ability to protect cells from heavy metal toxicity. NMR spectroscopy showed that NOON-2py forms complexes with Zn^{2+}, Cd^{2+}, and Hg^{2+} with similar conformations, whereas the Pb^{2+} and Ca^{2+} complexes attain different conformations. This result was corroborated by X-ray crystallography, which revealed the Cd^{2+} and Hg^{2+} complexes to be isomorphous, with both ions fully encapsulated in the diaza-18-crown-6 and the pendent pyridyl arms binding from opposite faces. By contrast, the Zn^{2+} crystal structure revealed a dinuclear species with two metal ions per ligand, and the Ca^{2+} structure showed this ion to sit on top of the 18-membered macrocycle. Further characterization of the Cd^{2+} complexes was provided by perturbed angular correlation (PAC) spectroscopy. Two distinct conformations of $[Cd(NOON\text{-}2py)]^{2+}$ were identified and based on density functional theory (DFT) calculations, these species were assigned to different δ/λ stereoisomers. Stability constants (log K_{ML}) showed NOON-2py to be remarkably selective for Cd^{2+}, Hg^{2+}, and Pb^{2+}, attaining values of 11.08, 21.46, and 11.67, respectively. For Ca^{2+} and Zn^{2+}, the log K_{ML} values of 3.62 and 6.83 are substantially smaller, reflecting a good thermodynamic selectivity of this chelator for the toxic metal ions. In vitro studies using HEK293T cells demonstrated that NOON-2py can preserve cell viability in cells treated with toxic concentrations of Cd^{2+}, Hg^{2+}, and Pb^{2+}. Fluorescence microscopy studies in HeLa cells using the Cd^{2+}- and Pb^{2+}-responsive fluorescent sensor Leadmium Green showed that NOON-2py can sequester intracellular deposits of these ions, reflecting the ability of this chelator to permeate cell membranes. Cd^{2+} and Pb^{2+} adsorbed on hydroxyapatite could be removed by NOON-2py within 15 min, suggesting that this chelator might

be valuable for the removal of these metal ions from bone. These results highlight the promise of NOON-2py as a new candidate for heavy metal decorporation that warrants further investigations in vivo.

Keywords: mercury, cadmium, lead, macrocycles, chelators

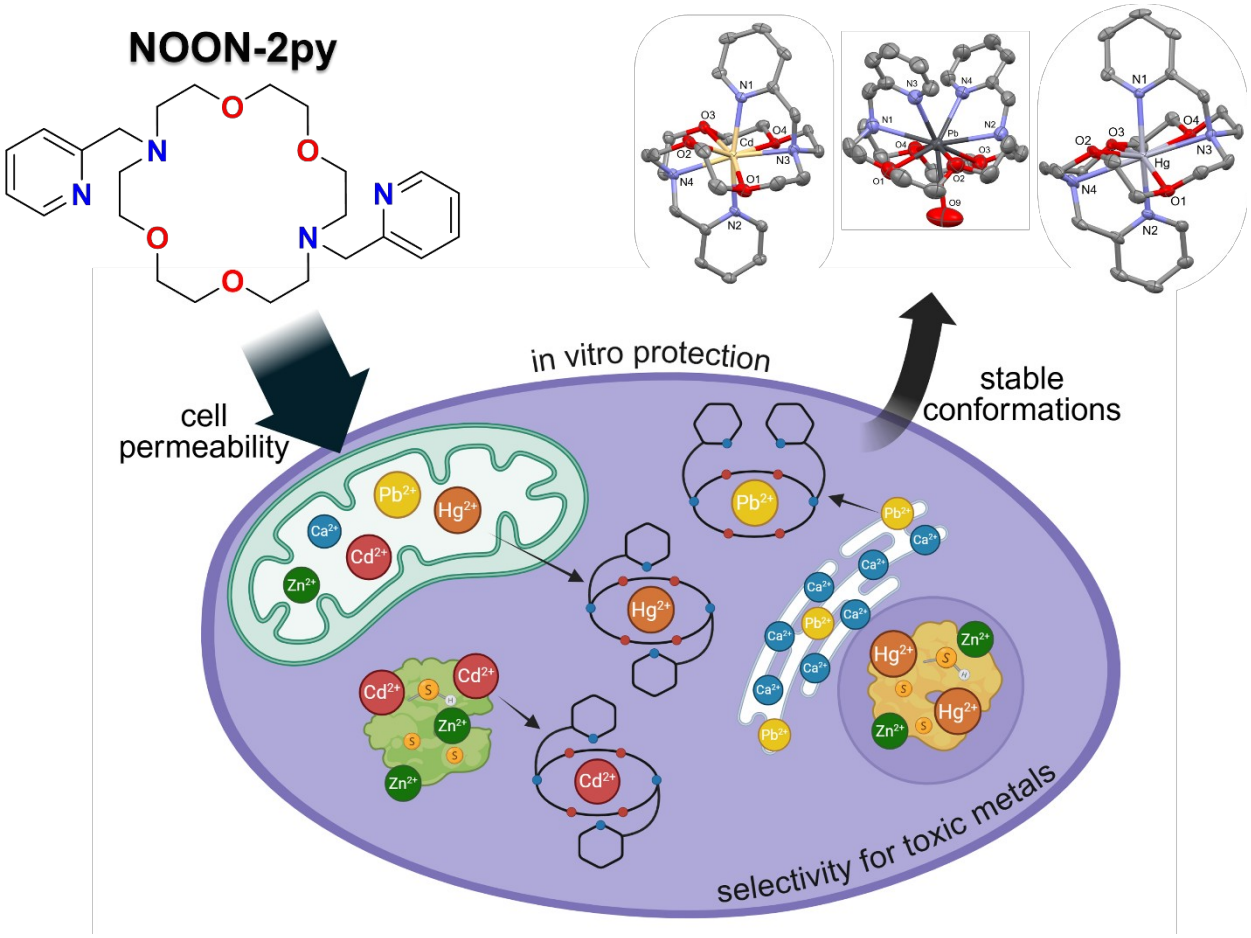

A diaza-18-crown-6 chelator appended with pyridyl pendant arms achieves highly stable, selective chelation of toxic heavy metals, Cd^{2+}, Hg^{2+}, and Pb^{2+}, and demonstrates in vitro sequestration of these metals, offering promise for chelation therapy.

1. Introduction

Cadmium (Cd^{2+}), mercury (Hg^{2+}), and lead (Pb^{2+}) are naturally occurring, highly abundant metals that are detrimental to human health.[1–3] Exposure to these heavy metals can occur via ingestion of contaminated foods or water, use of cigarettes or other tobacco sources, or inhalation of smoke from industrial fires or wildfires.[4–6] The damaging effects of heavy metal poisoning can vary dramatically, depending on exposure levels and duration, with symptoms ranging from nausea, birth defects, cognitive decline, to even death.[7] Heavy metal exposure is extremely prevalent; currently, 1 in 3 children globally have elevated blood Pb levels (>5 μg/dL).[8] Annually, since 2021, over 1.5 million deaths have been attributed to the effects of heavy metal poisoning by Cd^{2+}, Hg^{2+}, and Pb^{2+}.[8]

At the cellular level, these divalent metal ions exhibit similar chemical properties as endogenous calcium (Ca^{2+}) and zinc (Zn^{2+}).[3,9,10] Consequently, Cd^{2+}, Hg^{2+}, and Pb^{2+} leverage Ca^{2+} trafficking pathways, causing notable perturbations to mitochondrial function that dysregulate cellular processes and trigger apoptosis.[11–14] Additionally, these heavy metals strongly bind cysteine and methionine residues on proteins,[15–17] in accordance with their soft-to-borderline properties within Pearson's hard-soft acid-base theory.[18,19] Their high sulfur affinity contributes to their efficient capture by metallothioneins, and their subsequent delivery by this protein to the kidneys, resulting in their pronounced nephrotoxicity.[20] This impaired kidney function causes the depletion of electrolytes, primarily Ca^{2+}, which exacerbates the bone decalcification and demineralization triggered in cases of Pb^{2+} and Cd^{2+} poisoning.[21–23] Cd^{2+} and Pb^{2+} are also implicated in reproductive, cardiovascular, thyroid, and neurodegenerative disorders,[24–26] and Hg^{2+} is a known neurotoxin.[27,28] Given the perturbative effects of these metals on Ca^{2+}, treatment for heavy-metal toxicity must not further decrease concentrations of labile pools of key endogenous metal ions to avoid causing downstream damage characteristic of electrolyte depletion.[21,29]

To treat the effects of these toxic metal ions, chelation therapy is the most effective approach.[28,30] This strategy employs metal-binding chelators, which sequester and remove toxic metal ions via different excretion pathways.[31] Currently, there are 11 FDA-approved chelators for the treatment of Cd^{2+}, Hg^{2+}, or Pb^{2+} poisoning.[30] The most commonly prescribed are ethylenediaminetetraacetic acid (EDTA), dimercaptosuccinic acid (DMSA), and diethylenetriaminepentaacetic acid (DTPA) (**Chart 1**).[30] Among these chelators, EDTA is considered to be the gold standard. Its multiple donor atoms and flexible acyclic structure give rise to its remarkably high binding affinity for a wide range of metal ions. These effective metal-binding properties, however, present problems for its use in chelation therapy because it also binds and removes endogenous metal ions that are needed for normal biological function.[31,32] Consequently, EDTA treatment can cause significant side effects, including severe dehydration, hypocalcemia, and hypotension.[21,24,32] In addition, EDTA can increase Cd^{2+} and Pb^{2+} levels in the kidneys through the reuptake pathways, compounding nephrotoxicity.[21,32] Lastly, at physiological pH, EDTA is anionic and impermeable to cell

membranes, preventing it from removing toxic metal ions from intracellular environments and tissues.[31,32] Therefore, efforts to design more effective chelating agents that exhibit better selectivity for toxic metal ions and improved cell permeability are needed.

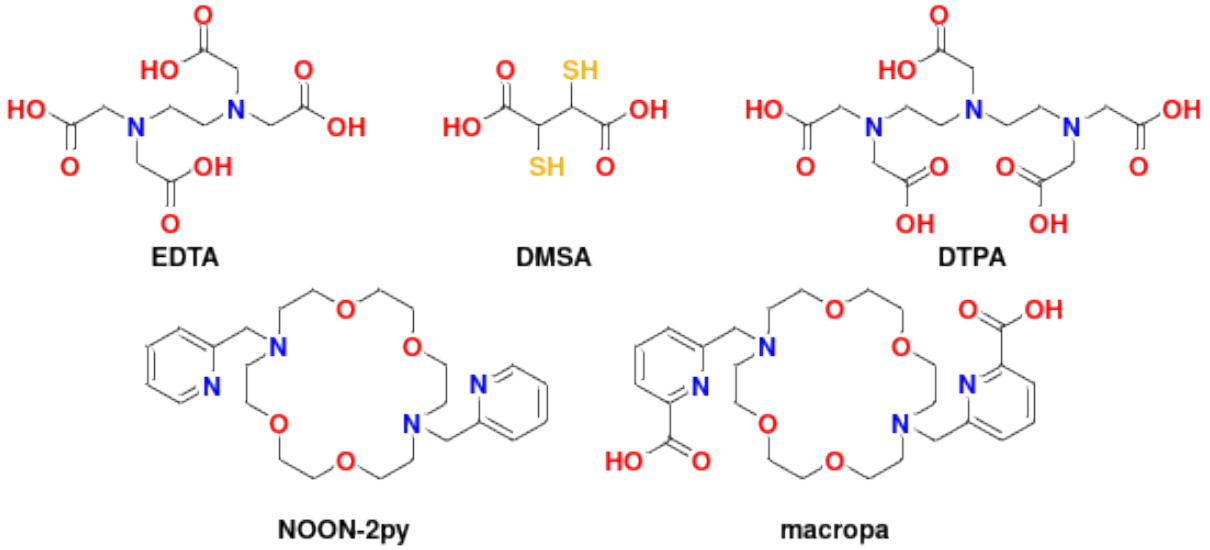

Chart 1. Chelators discussed in this work.

Toward this goal, several chelator design strategies have been employed for the sequestration of Cd^{2+}, Hg^{2+}, and Pb^{2+}, including the use of macrocyclic chelators with multiple sulfur donors designed to stabilize these soft metal ions.[33–36] Furthermore, recent interest in the ^{197m}Hg, ^{203}Pb, and ^{212}Pb radionuclides for nuclear medicine has led to novel selective chelators for Hg^{2+} and Pb^{2+}.[35,37–42] Although many of these chelators have been studied individually with Cd^{2+}, Hg^{2+}, or Pb^{2+}, most of them have not been investigated for their abilities to uniformly bind all of these metal ions. In this context, one of the major advantages of EDTA is that it is capable of decorporating all three toxic metal ions, Cd^{2+}, Hg^{2+}, and Pb^{2+}.[31,32] This broad-spectrum use of EDTA makes it effective in the clinic, where it can be prescribed to patients presenting with symptoms of heavy metal poisoning without needing to identify the specific ion. Thus, a chelator with broad-spectrum, high affinity for toxic heavy metals over endogenous metals would be a valuable clinical tool.

In targeting such a chelator, it is noteworthy that a common feature of Cd^{2+}, Hg^{2+}, and Pb^{2+}, which distinguishes them from endogenous metal ions, is their large 6-coordinate ionic radii of 0.95, 1.02, and 1.18 Å, respectively.[43] In this context, the well-known chelator macropa (6,6'-((1,4,10,13-tetraoxa-7,16-diazacyclooctadecane-7,16-diyl)bis(methylene))dipicolinic acid) (**Chart 1**) exhibits a distinct preference for binding large over small metal ions.[38,44–47] This binding preference is driven largely by its diaza-18-crown-6 macrocyclic core. As expected, macropa binds weakly to the endogenous Zn^{2+} ion (log K_{ZnL} = 9.23),[44] which has a small 6-coordinate ionic radius of 0.75 Å.[43] Perhaps unsurprisingly, macropa binds the large Pb^{2+} ion very effectively (log K_{PbL} = 16.23),[44] and this efficacy has prompted researchers to investigate macropa for nuclear medicine applications

involving radioisotopes of this metal ion.[38,48] An investigation of the coordination chemistry of macropa with Cd^{2+}, however, revealed that it formed a weak complex (log K_{CdL} = 8.95) and gave rise to a polymeric structure, where the Cd^{2+} center attained a 7-coordinate geometry that was not fully encapsulated in the macrocycle.[44] Hg^{2+} has not yet been studied by macropa, but we hypothesize the soft nature of this ion would be unfavorably matched to the chemically hard carboxylates of the pendent picolinate arms. These prior results prompted us to investigate an alternative to macropa that could stably and selectively bind the three evaluated toxic metal ions, Cd^{2+}, Hg^{2+}, and Pb^{2+}, over endogenous metal ions like Ca^{2+} and Zn^{2+}. Toward this goal, we investigated the previously reported chelator NOON-2py (7,16-bis(pyridin-2-ylmethyl)-1,4,10,13-tetraoxa-7,16-diazacyclooctadecane) (**Chart 1**).[40,49,50]

Like macropa, NOON-2py conserves the diaza-18-crown-6 macrocycle, maintaining its preference for binding to large metal ions.[47] In place of the anionic picolinate donors, NOON-2py employs pendant pyridyl groups, which are expected to be less effective donors for the chemically hard Ca^{2+} ion. In addition, the fewer donor atoms of NOON-2py compared to macropa should also stabilize the Cd^{2+} ion, which preferably attains coordination numbers of 7 or fewer. Lastly, the use of charge-neutral pyridyl groups increases the lipophilicity of this chelator over macropa and EDTA, potentially improving its ability for passive uptake in cells, marking a distinct advantage over anionic chelators. In this study, we evaluated the efficacy of NOON-2py and macropa as chelating agents for Cd^{2+}, Hg^{2+}, and Pb^{2+}, in comparison to the endogenous metal ions Ca^{2+} and Zn^{2+}, and their applications for the in vitro protection of human cells from these toxic metal ions.

2. Results and Discussion

2.1. Ligand and complex synthesis

The syntheses of NOON-2py and macropa have been previously reported.[40,45,49,50] NOON-2py is synthesized in a one-step alkylation of 2-bromomethylpyridine onto the macrocycle core 1,10-diaza-18-crown-6. NOON-2py was initially isolated as a dark oil, but after repeated extraction of the oil with hot hexanes, large pale-yellow crystals of the anhydrous free base form of this chelator were obtained from the mother liquor. Macropa was prepared as the 2HCl salt dihydrate, following the previously reported methods.[45,47] The syntheses of the Cd^{2+}, Hg^{2+}, Pb^{2+}, Ca^{2+}, and Zn^{2+} complexes were afforded by treating an aqueous solution of NOON-2py or macropa with the nitrate salts of these metal ions in aqueous solution. The complexes were isolated by lyophilization and further purified by crystallization. The Cd^{2+}, Hg^{2+}, and Pb^{2+} complexes with NOON-2py formed rapidly and quantitatively at room temperature in water and remain stable in solution and in solid state for over one year. The complexes were isolated as colorless solids that were characterized by elemental analysis and mass spectrometry. Within their mass spectra, the Cd^{2+}, Hg^{2+}, Pb^{2+}, and Ca^{2+} complexes revealed the major ion peak to have an *m/z* value corresponding to the $[ML]^{2+}$ species. Notably, within the mass spectrum of the Zn^{2+} complex, the major ion peak exhibited an *m/z* value

that could be assigned to the dinuclear $[M_2L(NO_3)_2]^{2+}$ species, suggesting that NOON-2py can accommodate two Zn^{2+} ions.

2.2. Nuclear magnetic resonance (NMR) spectroscopy of NOON-2py and macropa complexes

To characterize the complexes in aqueous solution, a combination of one-dimensional, two-dimensional, heteronuclear, and variable-temperature NMR spectroscopy was used. The ^{1}H NMR spectra of the NOON-2py ligand and its complexes of Cd^{2+}, Hg^{2+}, Pb^{2+}, Ca^{2+}, and Zn^{2+} are shown in **Figure 1**.

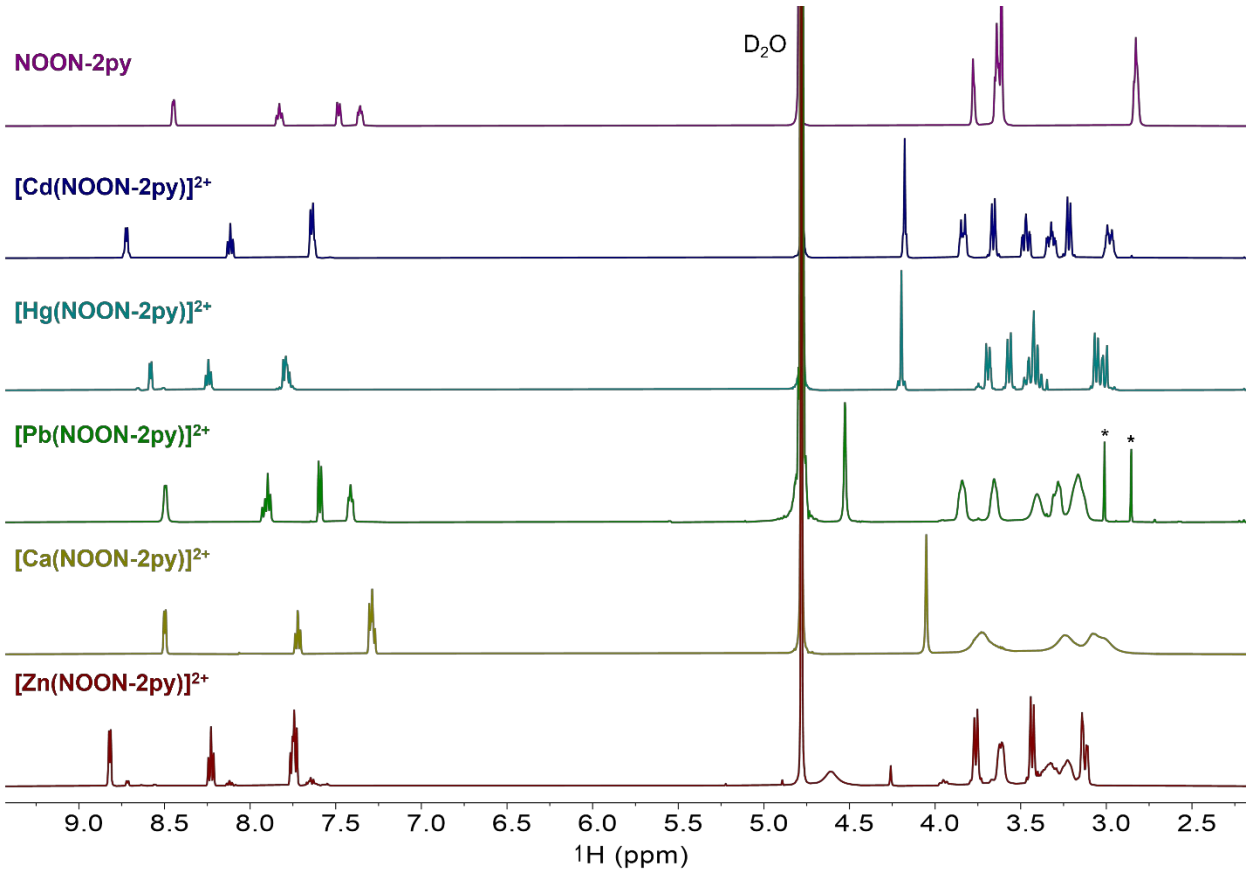

Figure 1. ^{1}H NMR spectra (500 MHz, T = 25 °C, D_2O, pD = 5.5) of [top to bottom] NOON-2py (purple), $[Cd(NOON\text{-}2py)]^{2+}$ (dark blue), $[Hg(NOON\text{-}2py)]^{2+}$ (light blue), $[Pb(NOON\text{-}2py)]^{2+}$ (green), $[Ca(NOON\text{-}2py)]^{2+}$ (yellow), and $[Zn(NOON\text{-}2py)]^{2+}$ (red). All metal complex spectra were acquired from a mixture of 1 equiv. $M(NO_3)_2{\cdot}nH_2O$ with 1 equiv. NOON-2py ligand. Asterisks denote residual dimethyl formamide (DMF) in the sample. Spectra are calibrated to acetonitrile internal standard at 2.06 ppm (not shown).

The ^{1}H NMR spectrum of NOON-2py reveals four resonances in the aromatic region arising from the H atoms on the pyridyl pendent arms. In the aliphatic region, a singlet at 3.81 ppm corresponds to the methylene CH_2 groups that connect the pendent pyridyl groups, and two triplets and a singlet are attributed to the protons on the macrocyclic ring. These resonances and those of the ^{13}C{^{1}H} NMR spectrum (**Figures S1–S2**) were fully assigned using an array of 2D NMR spectroscopic methods like ^{1}H-^{1}H COSY, ^{1}H-^{13}C HMBC, and ^{1}H-^{13}C HSQC (**Figures S3–S6**). The ^{15}N chemical shifts of the ligand were also determined using ^{1}H-^{15}N HMBC spectroscopy (**Figure S7**). This spectrum revealed the ^{15}N resonances of the nitrogen atoms on the pyridine to be at 298.6 ppm and the tertiary nitrogens of the macrocycle to be at 41.8 ppm (**Table 1**).

Table 1. NMR spectroscopic data for NOON-2py and investigated metal complexes.[a]

Compound	^{1}H py-*ortho* δ (ppm)[b]	^{1}H CH_2-arm δ (ppm)[b]	^{15}N py-N δ (ppm)[c]	^{15}N tertiary-N δ (ppm)[c]	Metal δ (ppm)
NOON-2py	8.45	3.78	298.6	41.8	n.a.[d]
$[Cd(NOON\text{-}2py)]^{2+}$	8.73	4.18	258.1	28.7	32.1[e]
$[Hg(NOON\text{-}2py)]^{2+}$	8.58	4.20	250.8	38.0	–1053[f]
$[Pb(NOON\text{-}2py)]^{2+}$	8.50	4.53	300.3	59.2	–2024[g]
$[Ca(NOON\text{-}2py)]^{2+}$	8.50	4.05	285.0	n.o.[h]	n.a.[d]
$[Zn(NOON\text{-}2py)]^{2+}$	8.82	4.61	243.9	n.o.[h]	n.a.[d]

[a]All spectra were acquired at 25 °C in D_2O (pD = 5.5). [b]Referenced to tetramethylsilane (δ = 0 ppm) based on an internal standard of MeCN at 2.06 ppm. [c]Referenced to $NH_3(l)$ at δ = 0 ppm. [d]Not applicable. [e]Cd-113 NMR signal referenced to a 0.1 M $Cd(ClO_4)_2$ in D_2O external sample at δ = 0 ppm. [f]Acquired with ^{1}H-^{199}Hg HMBC NMR spectroscopy; referenced to $HgMe_2$ at δ = 0 ppm, verified with a saturated $HgCl_2$ in D_2O external sample at δ = –1550 ppm. [g]Pb-207 NMR signal referenced to $PbMe_4$ at δ = 0 ppm, verified with an external sample of 1 M $Pb(NO_3)_2$ in D_2O at δ = –2960 ppm. [h]Not observed under these experimental conditions.

The Cd^{2+} complex of NOON-2py was characterized by multinuclear NMR spectroscopy as well, applying multi-dimensional spectroscopy to fully assign ^{1}H, ^{13}C, and ^{15}N resonances (**Figures S8–S13**). Upon complexation of Cd^{2+}, the ^{1}H NMR spectrum revealed a deshielding of the aromatic pyridine-based resonances, as well as diastereotopic splitting of the aliphatic resonances (**Figure 1**). This diastereotopic splitting, which is characteristic of complex formation, arises when the CH_2 protons become inequivalent, as distinguished by whether they attain an axial or equatorial positioning.[51] Although all of the CH_2 resonances on the macrocycle show this type of splitting, the CH_2 methylene resonances of pendent pyridyl group remain as a singlet. This result suggests that the protons on this methylene group are equivalent, at least on the NMR timescale. Another

noteworthy feature in the ^{1}H NMR spectrum of this complex is the observation of ^{1}H-^{113}Cd coupling. The I = ½ ^{113}Cd nucleus has a natural abundance of 12.22%, and consequently ^{1}H-^{113}Cd coupling appears in the form of satellite peaks (**Figure S8**). ^{113}Cd satellites are present on the ^{1}H resonances of protons on the *ortho* position of the coordinating pyridyl group and also within the CH_2 methylene protons. The ^{1}H-^{113}Cd coupling constants are $^{3}J_{CdH}$ = 8 and 16 Hz for the *ortho* and methylene protons, respectively. Additionally, the ^{13}C{^{1}H} NMR spectrum (**Figure S9**) also reveals the presence of ^{113}Cd satellite peaks. ^{13}C-^{113}Cd coupling is observed on the ^{13}C resonances corresponding to the *meta* and *ortho* protons on the pyridine pendant arms, and these have $^{3/2}J_{CdC}$ values of 54 and 80 Hz, respectively. The ^{15}N NMR chemical shifts of the complex were also measured, using ^{1}H-^{15}N HMBC NMR spectroscopy (**Figure S14**). The tertiary amine ^{15}N chemical shift is 28.7 ppm, whereas the pyridine nitrogen resonates at 258.1 ppm (**Table 1**). Notably, compared to the free ligand, the pyridine nitrogen is shifted 40.5 ppm upfield, whereas the tertiary amine only shifts upfield by 13.1 ppm upon coordination to Cd^{2+}. The more significant perturbation of the pyridine ^{15}N chemical shift may reflect a stronger interaction of the pyridyl nitrogen donor atoms with Cd^{2+} compared to the tertiary amine nitrogen. This result is consistent with the $^{3}J_{CdH}$ coupling observed for the ^{1}H NMR resonances corresponding to the pyridyl *ortho* and methylene hydrogen, but not within the protons residing on the macrocycle.

Lastly, the ^{113}Cd NMR chemical shift of the complex was measured via both a direct 1-D experiment and a 2-D ^{1}H-^{113}Cd HMBC NMR spectrum (**Figures S15–S16**). Both of these methods revealed the complex to possess a ^{113}Cd NMR chemical shift of 32.1 ppm (**Table 1**). This value is comparable to related Cd^{2+} complexes containing pyridine as a ligand.[52–54] The ^{1}H-^{113}Cd HMBC NMR spectrum showed the most intense cross peaks with the pyridine *ortho* proton and the methylene CH_2 group, consistent with our observation of ^{113}Cd satellites for these resonances within the ^{1}H NMR spectrum. Overall, these spectra indicate successful complexation of Cd^{2+} by NOON-2py in a conformationally locked, symmetrical geometry.

The multinuclear NMR spectra of the Hg^{2+} complex of NOON-2py were obtained and fully assigned using 2D NMR techniques (**Figures S17–S22**). The ^{1}H NMR spectrum of [Hg(NOON-2py)]$^{2+}$ is similar to that of the Cd^{2+}, revealing distinct diastereotopic splitting of the aliphatic protons and deshielding of the aromatic peaks (**Figure S17**). Also analogous to the Cd^{2+} complex is that the CH_2 methylene protons remain as a singlet, revealing their equivalence on the NMR timescale. Given the 16.8% natural abundance of the I = ½ ^{199}Hg nucleus, several resonances in the ^{1}H NMR spectrum also show satellite peaks, arising from ^{1}H-^{199}Hg coupling. The *ortho* hydrogens on the pyridine pendent arm exhibit a coupling constant $^{3}J_{HgH}$ of 74 Hz, whereas the methylene CH_2 resonances display satellite peaks with a $^{3}J_{HgH}$ = 20 Hz. Like the Cd^{2+} complex, the heteronuclear coupling constant is smaller for the methylene compared to the pyridine protons. The magnitude of these coupling constants and the absence of coupling with other protons on the macrocycle suggest that the Hg^{2+} ion is interacting more strongly with the two pyridine donors. Hg^{2+} often exhibits a stable linear 2-coordinate geometry,[55] thus the stronger interaction with the

pyridine donors on both sides of the macrocycle to give a pseudo 2-coordinate geometry is expected. These features are also manifested in the X-ray crystal structure (vide infra). Like the ^{1}H NMR spectrum, the ^{13}C{^{1}H} NMR spectrum of this complex (**Figure S18**) also reveals the complex to be symmetric, as reflected by the equivalency of resonances from the pyridine arms, indicating their chemically equivalent positioning. This complex was also amenable to characterization by ^{1}H-^{15}N HMBC NMR spectroscopy (**Figure S23**). These data revealed the pyridine nitrogen to have a ^{15}N chemical shift of 250.8 ppm and the tertiary amine nitrogen to have a chemical shift of 38.0 ppm (**Table 1**). These values are 47.8 and 3.8 ppm upfield from those of the free ligands, respectively. In comparison to that of the Cd^{2+} complex, the pyridyl nitrogen chemical shift is 7.3 ppm more shielded, and the aliphatic nitrogen chemical shift is 9.3 ppm less shielded. Thus, the nitrogen donors of the pyridine groups are more significantly perturbed in the Hg^{2+} complex compared to the Cd^{2+} complex. This result may suggest that Hg^{2+} interacts more strongly with these pyridines, while exhibiting weaker binding to the equatorial amines compared to the Cd^{2+} complex. This result is consistent with the preferred linear coordination geometry of Hg^{2+}.[55]

Lastly, the ^{199}Hg NMR spectroscopy of this complex was investigated. The ^{199}Hg chemical shift can span a wide range of values (–3000 to 500 ppm), reflecting the ability of ^{199}Hg NMR spectroscopy to be a sensitive probe for the interactions of this metal ion with different types of donor atoms.[39,56–61] Although we were unable to acquire a direct 1-D ^{199}Hg NMR spectrum of this complex, presumably due to significant line-broadening caused by fast relaxation afforded by coupling to the quadrupolar ^{14}N nuclei,[62] ^{1}H-^{199}Hg HMBC NMR spectroscopy was used to detect the ^{199}Hg chemical shift of this compound at –1053 ppm (**Figure S24**). This chemical shift is comparable to related Hg^{2+} complexes with four nitrogen donor atoms and substantially further downfield from that of aqueous $Hg(NO_3)_2$, which resonates at –2500 ppm.[58,59,63] The HMBC spectrum also showed clear strong correlations between the ^{199}Hg center and the *ortho* pyridine H atoms and the methylene CH_2 atoms, consistent with the satellite peaks observed in the ^{1}H NMR spectrum.

Although the Pb^{2+} complex of NOON-2py was previously studied by NMR spectroscopy,[40] we reinvestigated the NMR characterization of this complex (**Figures S25–S30**). A key distinction between the ^{1}H NMR spectrum of the Pb^{2+} complex, compared to the Cd^{2+} and Hg^{2+} complexes, lies within the aromatic region where clearly resolved individual signals are observed for each of the four protons on the pyridine. In addition, the aliphatic region shows the characteristic diastereotopic splitting, but the resonances themselves are substantially broadened relative to the Cd^{2+} and Hg^{2+} complexes. This broadening is most likely due to increased conformational flexibility of this complex. In addition, the methylene protons of the pendent pyridyl group remain as singlets, most likely reflecting fast arm rotational dynamics. ^{1}H-^{15}N HMBC NMR spectroscopy was also used to study this complex (**Figure S31**). The pyridine ^{15}N resonance appeared at 300.3 ppm and the aliphatic tertiary amine ^{15}N shift appeared at 59.2 ppm (**Table 1**). The aromatic shift is only 1.7 ppm downfield from the free ligand, whereas the aliphatic ^{15}N shift is 17.4 ppm downfield relative to the free ligand. The greater perturbation of the tertiary amine chemical shift compared to the

pyridine chemical shift is in contrast to our observations for the Cd^{2+} and Hg^{2+} complexes. This result suggests that Pb^{2+} interacts more strongly with the tertiary amines within the macrocycle compared to the pendent pyridine donors, marking a distinction from the coordination modes of this ligand with Cd^{2+} and Hg^{2+}. Finally, the ^{207}Pb NMR spectrum of this complex was measured (**Figure S32**). Both the 1-D ^{207}Pb and 2-D ^{1}H-^{207}Pb HMBC NMR spectra (**Figure S33**) revealed a ^{207}Pb NMR chemical shift at –2024 ppm, with the HMBC exhibiting cross-peaks with the *ortho* and *meta* pyridine protons, the methylene protons, and the aliphatic protons adjacent to the nitrogen heteroatoms and between the oxygen heteroatoms.

The NMR spectra of $[Ca(NOON\text{-}2py)]^{2+}$, which were fully assigned with 2D methods (**Figures S34–S38**), reveal distinct features compared to the heavy metal complexes discussed above. The ^{1}H NMR spectrum of this complex reveals similar chemical shifts within the aromatic region as those found within the spectra of the Cd^{2+} and Hg^{2+} complexes, in which two of the four resonances are overlapping. In the aliphatic region, the sharp singlet at 3.97 ppm corresponds to the methylene CH_2 on the pendant arms, whereas the macrocyclic CH_2 resonances are broad and lack diastereotopic splitting. These features reflect the conformational flexibility and dynamics of the complex, suggesting that it is less rigid than the heavy metal complexes discussed above. The ^{1}H-^{15}N HMBC NMR spectrum (**Figure S39**) could only successfully detect the ^{15}N resonance of the pyridine donor, which resonated at 285.0 ppm (**Table 1**). This value is shifted by 13.6 ppm relative to the free ligand.

Lastly, the NMR spectra of the NOON-2py complex of the endogenous ion Zn^{2+} were measured. As for other complexes, all spectra were assigned with an array of 2-D NMR techniques (**Figures S40–S44**). The ^{1}H NMR spectrum of a 1:1 mixture of Zn^{2+} and NOON-2py revealed the characteristic diastereotopic splitting in the aliphatic region, albeit with an unusual broadening of the methylene peak. The aromatic region of this spectrum is similar to that of the Cd^{2+}, Hg^{2+}, and Ca^{2+} complexes. In contrast to the other complexes investigated, however, the addition of an excess of Zn^{2+} (> 200 equiv.) led to a significant change in its NMR spectroscopic properties (**Figure S45–S48**). In the presence of excess Zn^{2+}, the ^{1}H NMR spectrum is shifted from that of the 1:1 mixture but still shows diastereotopic splitting within the aliphatic regions. Notably, the pyridyl methylene resonance appears as a sharp singlet within this solution. Based on the M:L stoichiometry, as well as crystallographic and potentiometric titrations (vide infra), this species is assigned as the 2:1 complex $[Zn_2(NOON\text{-}2py)]^{4+}$. As for the other complexes, the ^{15}N chemical shifts of these complexes were measured with ^{1}H-^{15}N HMBC NMR spectroscopy (**Figure S49**). The resonances of the pyridyl nitrogens, which occur at 243.9 ppm, are shifted upfield from the free ligand by 54.7 ppm (**Table 1**). This large shift signifies strong interactions with the pyridine donors. Similar to the Ca^{2+} complex, the Zn^{2+} complex ^{1}H-^{15}N HMBC also only shows peaks corresponding to the pyridine nitrogen. The absence of resonances from the aliphatic tertiary amines might be due to intensity loss from signal caused by fluxional behavior of the complex, as evidenced in part by the fact that NOON-2py is a weaker binder for Ca^{2+} and Zn^{2+}.

The NMR spectra of macropa and its complexes of these metal ion complexes were also studied for comparison to the NOON-2py system (**Figures S50–S55**). Among these complexes, those of Pb^{2+}, Cd^{2+}, and Zn^{2+} have previously been probed by NMR spectroscopy.[44] The ^{1}H NMR spectra of the Ca^{2+} and Cd^{2+} macropa complexes reveal no diastereotopic splitting within the aliphatic region. The other complexes of Pb^{2+}, Hg^{2+}, and Zn^{2+} show minor diastereotopic splitting, but the resonances within the aliphatic region are broad. Collectively, these results signify a greater conformational lability of the macropa complexes of these metal ions compared to those of NOON-2py.

2.3. X-ray crystal structures of NOON-2py and macropa complexes

Single crystals of NOON-2py and its complexes with Cd^{2+}, Hg^{2+}, Ca^{2+}, and Zn^{2+} were obtained and analyzed by X-ray diffraction (XRD) to determine their structures. The crystal structure of the Pb^{2+} complex of NOON-2py was previously reported, but its data are included and discussed here for comparison.[40] The crystal structure of the free base NOON-2py (**Figure 2a**, **Table S1**) reveals an open conformation of the macrocycle. NOON-2py has been previously crystallized as the protonated species in a cocrystal with two $[Na(NOON\text{-}2py)]^{+}$ complexes,[64] but never before as the free base ligand.

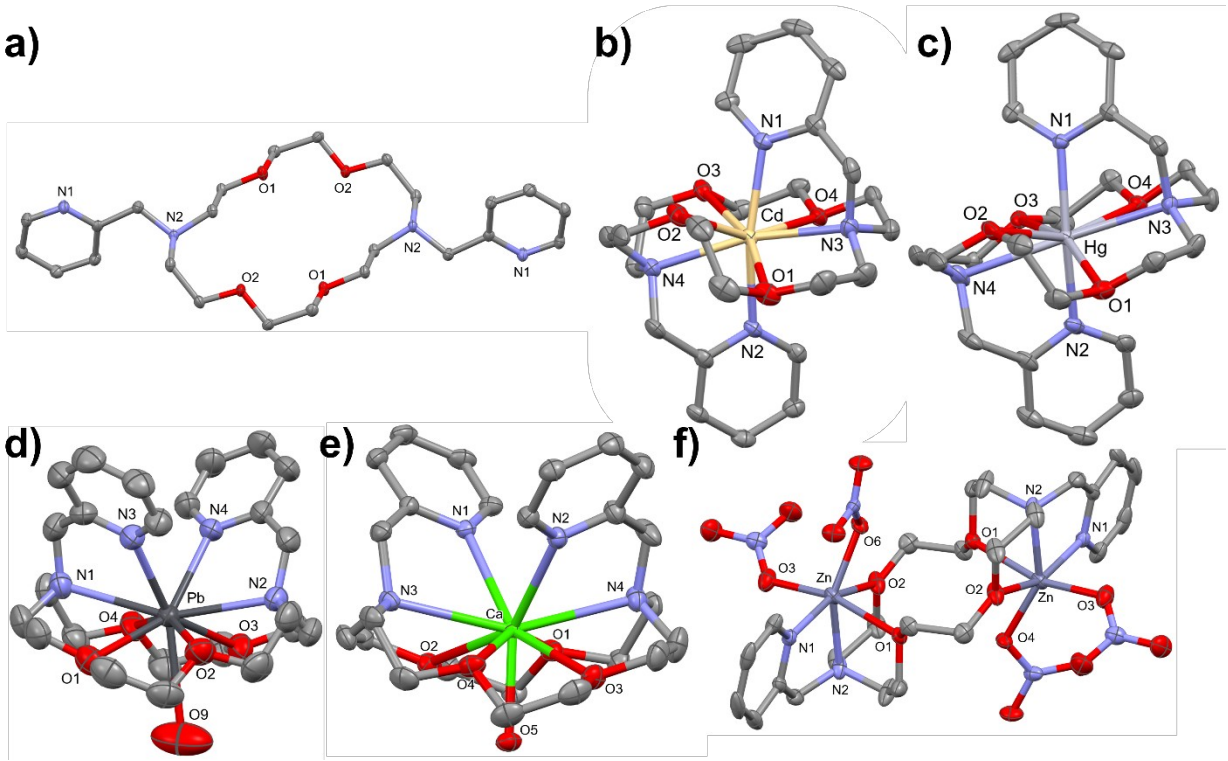

Figure 2. Crystal structures of (a) NOON-2py, (b) $[Cd(NOON\text{-}2py)]^{2+}$, (c) $[Hg(NOON\text{-}2py)]^{2+}$, (d) $[Pb(NOON\text{-}2py)(OH_2)]^{2+}$ from ref. 40, (e) $[Ca(NOON\text{-}2py)(OH_2)]^{2+}$, and (f) $[Zn_2(NOON\text{-}2py)(NO_3)_4]$. Thermal ellipsoids are drawn at the 50% probability level. Solvent, non-coordinating

counter ions, and hydrogen atoms are omitted for clarity. Atom colors are as follows: C = grey, N = blue, O = red, Cd = yellow, Hg = light grey, Pb = dark grey, Ca = green, Zn = slate. For $[Ca(NOON\text{-}2py)]^{2+}$, only one of the two complexes within the asymmetric unit is shown.

The crystal structure of $[Cd(NOON\text{-}2py)]^{2+}$ as its nitrate salt (**Figure 2b, Tables S2–S3**) reveals this complex to adopt a conformation in which the Cd^{2+} center is fully encapsulated in the macrocycle with the pyridine pendant arms positioned axially above and below the plane of the macrocycle. In this conformation, the Cd^{2+} center is 8-coordinate and coordinatively saturated. The overall conformation of the macrocycle upon coordination can be described using the δ and λ notation,[65,66] which convey the chirality found within each five-membered chelate ring. For this structure, the NOON-2py attains the (δδδ)(δδλ) conformation. The N–Cd–N interatomic angle of the pyridine nitrogens is 162.62°, marking a deviation from perfect linearity. Consequently, this structure indicates that the CH_2 methylene H atoms are inequivalent in the solid-state, a feature that was not observed within the ^{1}H NMR spectrum of this complex, which shows resonances for these protons that appear as a singlet. The Cd–N interatomic distances are shorter for the pyridine nitrogens compared to the aliphatic coordinating nitrogens (2.312 and 2.278 Å vs. 2.432 and 2.469 Å). This result is consistent with the ^{15}N NMR chemical shift data, which shows more significant perturbation of the pyridine N chemical shifts compared to those of the tertiary amines.

The crystal structure of $[Hg(NOON\text{-}2py)]^{2+}$ is isomorphous to that of the $[Cd(NOON\text{-}2py)]^{2+}$ complex, crystallizing with the same coordination geometry, space group, and nearly identical unit cell parameters (**Figure 2c**, **Tables S4–S5**). Like within the Cd^{2+} structure, the Hg^{2+} ion attains an 8-coordinate geometry, with the two pyridines binding from above and below the macrocycle plane with a non-linear pyridine–Hg–pyridine interatomic angle of 164.46°. The Hg–N distances between the pyridine donors are 2.183 and 2.191 Å, shorter than the tertiary amine Hg–N distances of 2.566 and 2.595 Å. These results are consistent with the larger perturbation of the ^{15}N chemical shifts of the pyridine nitrogen compared to the very minimal change in the ^{15}N chemical shifts of the tertiary amines. The difference in Hg–N distances between the axial pyridines and equatorial amines is also significantly larger than that observed within the isomorphous Cd^{2+} complex. The differences between the average of the two aromatic M–N bonds between the Cd^{2+} and Hg^{2+} complexes are $\Delta d = 0.108$ Å, and the differences between the average of the two aliphatic M–N bonds between the Cd^{2+} and Hg^{2+} complexes are $\Delta d = -0.130$ Å. The much stronger axial Hg–N interactions compared to Cd–N interactions may be a consequence of the strong preference for the Hg^{2+} ion to attain a linear 2-coordinate geometry.[55] Lastly, the macrocycle conformation attains a mixture of the (δδδ)(δδλ) and (δδδ)(δλλ) forms, which are both present as reflected by crystallographic disorder, consistent with the symmetry observed in the ^{1}H NMR spectrum.

The structure of $[Pb(NOON\text{-}2py)(OH_2)]^{2+}$ (**Figure 2d**) was previously determined by X-ray crystallography.[40] The structure adopts a conformation in which the Pb^{2+} ion is slightly above the

plane of the macrocycle and both pyridine pendant arm donors are positioned above the plane of the macrocycle, on the same face of the Pb^{2+} ion. In the axial position below the plane of the macrocycle, there is an inner-sphere water molecule bound. The Ca^{2+} complex of NOON-2py crystallizes in a similar conformation as the Pb^{2+} complex (**Figure 2e**, **Tables S6–S7**). In this structure, which contains two structurally similar complexes within the asymmetric unit, the Ca^{2+} ion sits on top of the diaza-18-crown-6 macrocycle, and the two pendent pyridine groups bind on the same face. In addition, an inner-sphere water ligand interpenetrates through the macrocycle, leading to a 9-coordinate Ca^{2+} center. The axial Ca–OH_2 distances of the complexes are 2.342 and 2.348 Å. The pyridine Ca–N distances range from 2.577 to 2.610 Å, whereas the Ca–N distances with the tertiary amines are longer, ranging from 2.716 to 2.738 Å. The Ca–O distances of the macrocycle ethers range from 2.552 to 2.637 Å. Finally, the chirality of the macrocycle conformation is identical in both complexes in the asymmetric unit. The macrocycle attains the Λ(δλδ)(δλδ) conformation identical to the Pb^{2+} complex of NOON-2py, where Λ signifies the pendent arm helical chirality. The two complexes in the asymmetric unit are connected by a network of hydrogen-bonding water molecules and nitrate counterions between the two axially positioned waters.

Crystals grown from a mixture of $Zn(NO_3)_2$ and NOON-2py were revealed by X-ray diffraction to be the dinuclear complex, $[(NO_3)_2Zn(NOON\text{-}2py)Zn(NO_3)_2]$ (**Figure 2f**, **Tables S8–S9**). In this structure, the symmetry-equivalent Zn^{2+} ions attain a 6-coordinate distorted octahedral geometry. The coordination sphere is completed by two monodentate nitrates, the pyridine nitrogen, the tertiary amine nitrogen, and two of the macrocycle ether oxygens. This structure shows that the Zn^{2+} ions bind on the exterior of the macrocycle, reflecting the hypothesized size mismatch between the macrocycle core and metal ionic radius. The asymmetric unit only contains half the macrocycle and one coordinated Zn atom. Although there is disorder within the nitrate ligands, the Zn–O distances (2.061–2.031 Å) are clearly much shorter than the Zn–O distances (2.405–2.361 Å) arising from the macrocycle ethers. Importantly, this dinuclear crystal structure is consistent with our observation by NMR spectroscopy, where the addition of greater than two equivalents of Zn^{2+} led to the formation of this complex.

For comparison, a discussion of previously reported crystal structures of the macropa complexes of Zn^{2+}, Cd^{2+}, and Pb^{2+} is warranted.[44] For the Cd^{2+} structure, the metal ion is not fully incorporated into the macrocycle, but instead forms a polymeric structure where the 7-coordinate Cd^{2+} ion is bound to two picolinate arms of adjacent ligands, one nitrogen and one oxygen on the macrocycle, and a chloride ion. The Zn^{2+} structure of macropa reveals a 5-coordinate structure, where the primary coordination sphere comprises two bidentate picolinate arms and a water molecule. In this case, the Zn^{2+} ion resides above the diaza-18-crown-6 macrocycle, which forms hydrogen-bonding interactions with the bound water. Lastly, the crystal structure of the Pb^{2+} complex of macropa shows an ideal interaction. In this complex, the 10-coordinate Pb^{2+} ion sits on top of the macrocycle with both pendent picolinate arms binding from the same face. The structures of both the Zn^{2+} and

Cd^{2+} macropa complexes reveal that these metal ions are not appropriately matched to this ligand, based on their ionic radii and preferred coordination numbers, whereas the Pb^{2+} is suitable. Thus, macropa is a good ligand for Pb^{2+} but not Cd^{2+}, limiting its potential use for sequestering toxic metal ions. By contrast, NOON-2py forms discrete 1:1 complexes with both Pb^{2+} and Cd^{2+}, marking a potential advantage of this ligand for broad-spectrum heavy metal removal as verified by potentiometric studies described below.

2.4. Perturbed angular correlation (PAC) spectroscopy and density functional theory (DFT) analysis

To further characterize the Cd^{2+} complex of NOON-2py, we used perturbed angular correlation (PAC) spectroscopy. This method relies on the use of a suitable radioisotope to measure the angular correlation between two sequentially emitted gamma photons. This correlation reveals information on the coordination environment of the radioactive metal ion within around a 3–5 Å radius. In this case, ^{111m}Cd is particularly suitable for this application based on its decay properties that lead to sequential gamma photon emission through a transient nuclear excited state with an appropriate lifetime. This method has previously been applied for bioinorganic chemistry, where the ^{111m}Cd nucleus has been substituted into Zn metalloproteins.[67–70] In this work, we demonstrate the use of PAC spectroscopy as a tool for the evaluation of this small-molecule system, specifically in the elucidation of conformers that explain the discrepancy with the symmetry observed for the methylene peaks by ^{1}H NMR and the asymmetry observed for the methylene protons by XRD.

Five parameters (A, η, ω_0, δ, and $1/\tau_c$) can be determined for each ^{111m}Cd site (**Table 2**). Of these parameters, two of them, the nuclear quadrupole interaction (NQI) strength, ω_0, and the asymmetry parameter, η, directly reflect the structure at the metal site.[67] In an axially symmetric structure, η is 0, whereas for maximally non-axially symmetric complexes, this value is 1. Both ω_0 and η can be calculated for a given molecular structure using first principles quantum mechanical methods or using semi-empirical models.[67] The amplitude of the signal, A, depends on properties of the nuclear decay and on the sample-detector geometry.[67] If more than one structure at the site of the PAC probe is present, the relative amplitudes will, in general, directly reflect the relative population of the different sites.

The linewidth of the Fourier-transformed data is affected by structural variations at the site of the PAC probe from one molecule to the next, reflected in the relative peak width δ. Thus, δ qualitatively reflects the structural flexibility at the site of the PAC probe. Dynamics similarly affects the PAC signal, and is reflected in the parameter $1/\tau_c$, where τ_c is the rotational correlation time of Brownian tumbling.[71]

For a spin 5/2 nucleus, which is the case for the relevant nuclear level of ^{111m}Cd, one NQI manifests itself as three peaks in the Fourier transform of the PAC data. The frequencies of the three peaks are not independent, because the sum of the two lowest frequencies must add up to the third: $\omega_1 + \omega_2 =$

ω_3.[67] For samples with randomly oriented molecules, which is the case in solution and powder crystals, the intensity distribution of the three peaks from each signal is such that the lowest frequency peak (ω_1) has the highest intensity, the second (ω_2) has intermediate intensity, and the third (ω_3) has the lowest intensity.[67]

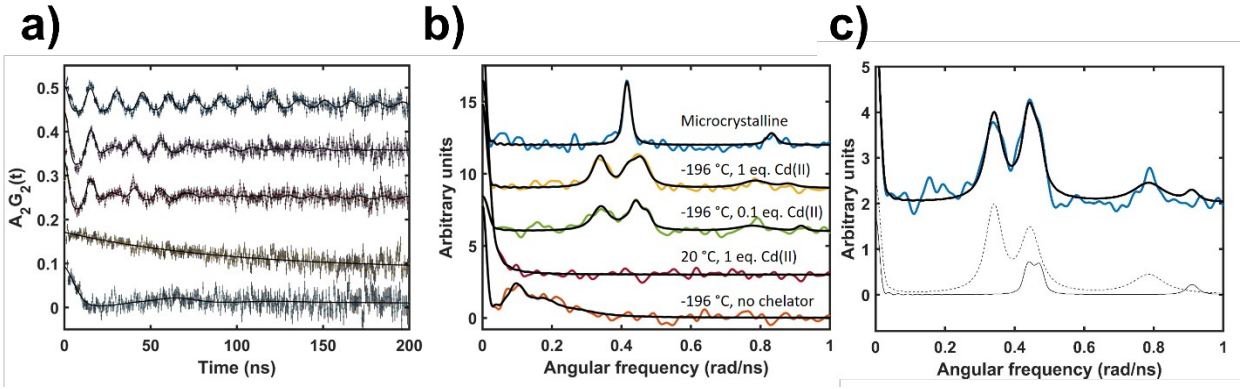

Figure 3. ^{111m}Cd PAC spectroscopy data for $[Cd(NOON\text{-}2py)]^{2+}$ complexes. (a) Experimental data (colored data points with error bars) and fitted perturbation function (black line). Samples are, in descending order, the microcrystalline sample, frozen solution at –196 °C with 1 equiv. Cd^{2+}, frozen solution at –196 °C with 0.1 equiv. Cd^{2+}, solution at 20 °C with 1 equiv. Cd^{2+}, and frozen solution at –196 °C with no chelator added. (b) Fourier transformed data (colored line) and fit (black line). (c) Decomposition of the ^{111m}Cd PAC signal from the $[Cd(NOON\text{-}2py)]^{2+}$ samples in frozen solution (–196 °C) into two NQIs. Top: Fourier transform of the sum of the experiments recorded on the $[Cd(NOON\text{-}2py)]^{2+}$ in frozen solution, with data shown as the blue line and the fit shown as the black line; bottom: decomposition of the fit into the two constituent NQIs. NQI1 (dashed line) was fit with $\omega_0 = 0.240$ rad/ns and $\eta = 0.688$, and NQI2 (solid line) was fit with $\omega_0 = 0.263$ rad/ns and $\eta = 0.92$, see **Table 2**.

The PAC spectra of $[Cd(NOON\text{-}2py)]^{2+}$ were investigated in both the solid-state as well as in frozen and room temperature solutions. The frozen (–196 °C) solution-phase measurements were carried out using both a 1:1 and 1:10 metal-to-ligand ratio, giving nearly identical results with both conditions and allowing their data to be added to improve signal-to-noise. An analogously made solid-state sample was confirmed to be microcrystalline and of the same polymorph as the single-crystal X-ray structure discussed above via powder X-ray diffraction (**Figure S56**). $[Cd(NOON\text{-}2py)]^{2+}$ was confirmed to be stable across a range of pH values (5.5–9) used in the PAC experimental procedure (**Figure S57**). As a comparative control, the PAC spectrum of free aqueous Cd^{2+} was also measured in frozen solution, revealing a significantly different spectrum from any of the NOON-2py-containing samples. Lastly, an additional experiment was conducted on a 10:1 NOON-2py-to-Cd^{2+} sample in aqueous solution at 20 ºC. These data displayed the expected

exponential decay signature of the perturbation function, reflecting rapid rotational diffusion of the complex.

The PAC spectrum of the solid microcrystalline $[Cd(NOON\text{-}2py)]^{2+}$ revealed a single NQI, characterized by $\omega_0 = 0.236$ rad/ns with η fixed at 1.0. By contrast, the complex in frozen aqueous solution is more complex and cannot be fitted reliably with only one NQI. Qualitatively, this conclusion is based on the fact that the second peak (ω_2) is more intense than the first peak (ω_1), and these intensities are in conflict with PAC theory for a single NQI for randomly oriented molecules.[67] These data, instead, are best analyzed with two NQIs, as illustrated in **Figure 3c**, and the fitted parameters are presented in **Table 2**. One NQI (NQI1, $\omega_0 = 0.240$ rad/ns, $\eta = 0.688$) is easily identified, because all three peaks are observed at 0.35 rad/ns, 0.45 rad/ns, and 0.80 rad/ns, and they obey the physical requirement of $\omega_1 + \omega_2 = \omega_3$. The frequency, $\omega_0 = 0.240$ rad/ns, is similar to the frequency observed for the microcrystalline sample, but the asymmetry parameter, η, is significantly smaller than that of the microcrystalline sample. The key implication of these frozen solution PAC spectra is that the complex is present in two distinct conformations under these conditions.

Table 2. Summary of parameters fitted to ^{111m}Cd PAC data for $[Cd(NOON\text{-}2py)]^{2+}$ in the microcrystalline state and in frozen solution. Two NQIs, NQI1 and NQI2, reflecting two co-existing species, were fit to the PAC data recorded for $[Cd(NOON\text{-}2py)]^{2+}$ in solution.

Experiment	ω_0 (rad/ns)	η	δ ×100	$1/\tau_c$ (μs^{-1})	A ×100	χ_r^2
Microcrystalline	0.2360(4)	1.0[a]	1.2(4)	3(1)	5.0(3)[b]	0.82
NQI1 (–196 °C)	0.240f	0.688(8)	6.4(7)	2.2(4)	9.0(6)	0.81
NQI2 (–196 °C)	0.263(2)	0.92(1)	1.4(8)	2.2(4)	1.8(3)	0.81

[a]Fixed. [b]Lower total amplitude, A, than the other experiment due to a shorter sample-detector distance.

To probe the identity of the two conformations in more detail, variable-temperature NMR spectroscopy of $[Cd(NOON\text{-}2py)]^{2+}$ was carried out. As noted above, the room-temperature NMR spectra of this complex convey the presence of a single isomer that is fairly rigid based on diastereotopic differences between macrocycle proton resonances. Notably, the pyridyl methylene CH_2 resonance appears as a singlet, reflecting an arm-wagging motion that is fast on the NMR timescale. An analysis of this complex by ^{1}H NMR spectroscopy in methanol-d_4 at temperatures as low as –80 °C revealed a general broadening of the aliphatic resonances, including the methylene CH_2 group (**Figure S58**). This result suggests that at this temperature the resonances start to

deconvolute into distinct conformations, like those observed by PAC spectroscopy. In any case, the inability to fully resolve these distinct species even at –80 °C reflects the very fast rate of their interconversion, which is uniquely probed by PAC spectroscopy.

To investigate the two possible conformations in more detail, density functional theory (DFT) was employed. Specifically, we sought to optimize the geometries and determine the relative free energy values (ΔG) of the different conformers of $[Cd(NOON\text{-}2py)]^{2+}$ with different combinations of δ and λ chelate ring chirality. The energies of these conformers are collected in **Table S10**. Geometries with a single δ/λ switch on the macrocycle in comparison to the crystal structure of the $[Cd(NOON\text{-}2py)]^{2+}$ complex were the most stable. Attempts to optimize conformational geometries with many alterations of the δ/λ stereochemistry led back to geometries that matched the crystal structure, with the exception of the (δδδ)(δλλ) and (δδδ)(λδλ) conformations for which stable local minima could be identified. With these different conformation geometries, their PAC parameters were calculated with DFT (**Table S11**). The NQI parameters of the (δδδ)(δλλ) conformer (ω_0 = 0.251 rad/ns, η = 0.63) match the experimental values well for NQI1. This result suggests that this is the major conformer observed by PAC spectroscopy. The other species, NQI2, can be reasonably assigned to the (δδδ)(δδλ) conformer (ω_0 = 0.241, η = 0.87), consistent with the crystal structure of the complex. These assignments are based on the similarity in the η and ω_0 PAC parameters and the relatively low energy of these conformations. Overall, PAC spectroscopy was used to identify the presence of two conformations of $[Cd(NOON\text{-}2py)]^{2+}$ in solution, while only a single species could be detected by both NMR and XRD. As shown by DFT, these conformations are very close in energy and consequently are also likely to interconvert very rapidly in solution. Thus, PAC spectroscopy can resolve these energetically and chemically similar conformations that could not be identified with X-ray diffraction or NMR spectroscopy alone.[72]

2.5. Thermodynamic stability constants

To evaluate the potential of NOON-2py for the selective binding of the toxic heavy metal ions, Cd^{2+}, Hg^{2+}, and Pb^{2+}, over the endogenous Ca^{2+} and Zn^{2+} ions, the stability constants (log K_{ML}) of these complexes were determined via potentiometric titrations.

Table 3. Protonation constants of NOON-2py, macropa, and EDTA and thermodynamic stability constants of their Cd^{2+}, Hg^{2+}, Pb^{2+}, Ca^{2+}, and Zn^{2+} complexes in solution.

	NOON-2py	macropa[a]	EDTA[b]
log K_{a1}	7.46(3), [7.44][c]	7.52	10.17
log K_{a2}	6.22(3), [6.26][c]	7.03	6.11
log K_{a3}	1.96(1), [1.38][c]	3.58	2.68
log K_{a4}		2.47	2.00
log K_{a5}			1.50
log K_{CdL}	11.08(2)	8.95	16.39
log K_{CdHL}		6.03	2.90
log K_{HgL}	21.46(3)[d]	9.08(1)	21.50
log K_{HgHL}		6.15(12)	3.10
log K_{PbL}	11.67[e]	16.23	17.88
log K_{PbHL}		2.86	
log K_{CaL}	3.62(5)	5.25	10.61
log K_{ZnL}	6.83(2)	9.23	16.44
log K_{ZnHL}		6.77	3.00
log K_{ZnH2L}		2.89	
log K_{Zn2L}	8.69(7)		
pCd	11.73	9.57	14.62
pHg	25.00	9.72	19.73
pPb	12.29	17.11	16.37
pCa	6.01	6.24	8.84
pZn	7.48	9.86	14.68

[a]Ref 44. [b]Ref [73]. [c]Ref 49. All constants evaluated were determined at I = 0.1 M KNO_3 or [d]I = 0.1 M KCl at T = 25 °C. [d]The model for the log K_{HgL} determination included the stability constants for $HgCl_x$ species as follows: log K_{HgCl+} = 6.72, log K_{HgCl2} = 13.23, log K_{HgCl3-} = 1.0, log $K_{HgCl4-2}$ = 1.97.[75] [e]Ref. 40 pM = –log $[M^{2+}]_{free}$. Calculated for 10 μM total ligand and 1 μM total metal at pH 7.4 and 25 °C. Values in parentheses are the standard deviation between three replicates.

Prior to determining metal complex stability constants, accurate values for the protonation constants of NOON-2py are required. The protonation constants of this ligand were previously measured by potentiometric titrations,[49] and these values are shown in **Table 3**. Here, we investigated NOON-2py by potentiometric and UV-vis titrations (**Figures S59–S61**). The first two protonation constants measured by the potentiometric titrations are 7.46 and 6.22, and they

correspond to the deprotonation of the tertiary amines on the macrocycle. These values are consistent with the previously reported first and second protonation constants of this ligand as determined by potentiometric titrations.[49] However, this earlier study also reported a third protonation constant with a value of 1.38. Within our potentiometric titrations, however, the electrode is calibrated only between a pH range of 2.2–11.3. Consequently, our attempts to include this third acidic protonation constant in our model gave unreliable values ranging between 1.2 to 2.5. To more accurately determine this third protonation constant, UV-vis titrations in the acidic pH range of 1.30 to 2.48 were carried out. These data reliably converged to a value of 1.96, slightly larger than the previously reported value. Using these protonation constants, the stability constants were determined.

The potentiometric titrations of Cd^{2+}, Hg^{2+}, Ca^{2+}, and Zn^{2+} were performed using potassium nitrate (0.1 M) as the supporting electrolyte and HNO_3 as the titrant. The use of nitrate and HNO_3 was chosen over KCl and HCl to avoid having to account for the non-negligible binding constants of Zn^{2+} and Hg^{2+} with the halides.[74–76] The potentiometric titration data of the Cd^{2+} and Ca^{2+} complexes were best fit with a single 1:1 ML species (**Figures S62–S63**), and the resulting log K_{ML} values are collected in **Table 3**. For the Zn^{2+} titrations, however, the data were best fit via the inclusion of a 2:1 M_2L species in the solution equilibria. Notably, this stoichiometry is consistent with both our crystal structure and NMR spectroscopy studies of this complex (**Figure S64**).

Attempts to carry out potentiometric titrations with Hg^{2+} and NOON-2py were unsuccessful with KNO_3 as the supporting electrolyte, as quantitative complex formation was found even at the lowest pH value (~2) of our titration. From these potentiometric titrations, a lower limit for the $[Hg(NOON\text{-}2py)]^{2+}$ log K_{ML} value was estimated to be 20. In an attempt to circumvent this issue, we carried out an NMR titration with HNO_3 in a low pH regime. Even at pH = 0.54, however, the complex remained intact (**Figure S65**). To solve this problem, we carried out a potentiometric pH titration using HCl in the presence of 0.1 M KCl as the supporting electrolyte. Under these conditions, we could leverage the competitive equilibrium for the formation of $HgCl_2$ in order to titrate over conditions in which complex dissociation is observed. Analysis of the pH potentiometric titration under these conditions with the inclusion of the $HgCl^+$ and $HgCl_2$ formation constants within our model led to satisfactory refinement, enabling us to determine the log K_{HgL} value of 21.46 (**Figure S66**). This approach of using the competitive equilibrium involving Cl^- was further verified by NMR spectroscopy. The adjustment of a solution of $[Hg(NOON\text{-}2py)]^{2+}$ to pH 2.2 and below with HCl enabled detection of free ligand (**Figure S67**).

Because the stability constant of the Hg^{2+} complex of macropa has not yet been determined, we also investigated this system by potentiometric titration. These data revealed the Hg^{2+} complex of macropa to be significantly less stable than that of NOON-2py. Consequently, log K_{ML} and log K_{MLH} values could be accurately obtained via fitting of the potentiometric data with KNO_3 as the supporting electrolyte and HNO_3 as the titrant (**Figure S68**). The log K_{ML} value of the Hg^{2+} complex

of macropa (9.08) is significantly smaller than that of the NOON-2py complex, reflecting the poor affinity of macropa for this metal ion.

A comparison of the stability constants of NOON-2py, macropa, and EDTA under physiologically relevant conditions can be made using pM values, the $-\log[M]_{free}$ under the previously reported conditions of 1 μM M^{2+} and 10 μM L at pH 7.4.[40] As shown in **Table 3**, the pM values of NOON-2py for Cd^{2+}, Hg^{2+}, and Pb^{2+} are 11.73, 25, and 12.29, respectively. Importantly, these pM values are substantially greater than those for Ca^{2+} and Zn^{2+}, which only reach values of 6.01 and 7.48, respectively. This result indicates that NOON-2py has a remarkable selectivity for toxic metal ions over these endogenous ions. By comparison, EDTA exhibits poor selectivity between Zn^{2+} (pZn = 14.68) and Cd^{2+}, Hg^{2+}, and Pb^{2+}, for which the pM values are 14.62, 19.73, and 16.37, respectively. This property is consistent with some of the known toxic side effects of EDTA that arise from depletion of biological Zn^{2+} levels.[31,77] Macropa, on the other hand, exhibits a very high selectivity for Pb^{2+} (pPb = 17.11) over the other metal ions studied here. These results suggest that macropa would be a promising candidate for Pb^{2+} decorporation. However, the poor selectivity of macropa for Cd^{2+} and Hg^{2+} over Zn^{2+} and Ca^{2+} suggests that it would not be effective for removing these other two toxic metal ions. In this context, the data obtained for NOON-2py suggest that NOON-2py could be valuable as a broad-spectrum decorporation agent for Cd^{2+}, Hg^{2+}, and Pb^{2+}.

2.6. Cytotoxicity, cell viability protection, and cell uptake

Based on the good selectivity of NOON-2py for Cd^{2+}, Hg^{2+}, and Pb^{2+}, it was evaluated in a series of in vitro cell assays to determine its ability to protect cells from heavy metal-mediated toxicity. First, the cytotoxicity of the free ligands and uncomplexed metal ions was measured in HEK293T cells, a human kidney fibroblast cell line that is relevant due to the known nephrotoxicity of Cd^{2+}, Hg^{2+}, and Pb^{2+}.[20,22] After treating HEK293T cells with various doses of these metal ions for 48 h, the (4,5-dimethylthiazol-2-yl)-2,5-diphenyltetrazolium bromide (MTT) assay was used to determine their IC_{50} values, which fall within the range of 0.5–10 μM (**Figures S69–S71**, **Table S12**). The cytotoxicity of the free ligands NOON-2py, macropa, and EDTA was also measured; both EDTA and macropa are non-toxic at concentrations greater than 1 mM, whereas the IC_{50} value of NOON-2py was found to be 64 μM (**Figures S72–S74**, **Table S12**). The mild toxicity may also be attributed to the increased lipophilicity of NOON-2py compared to macropa and EDTA, enabling greater uptake of the chelator into the cells. Although NOON-2py is more cytotoxic than both EDTA and macropa, its IC_{50} value is still larger than typical concentrations applied for decorporation, both in vivo and in vitro. For example, we roughly calculated that with an administered dose of 1000 mg/m^2 and a 0.3 partition coefficient for the kidneys,[31] assuming average body surface area of 1.73 m^2 and water content of 42 L, that the maximum concentration of EDTA in the kidneys would be 33 μM. In this context, NOON-2py is still a viable decorporation agent when used at appropriately low doses.

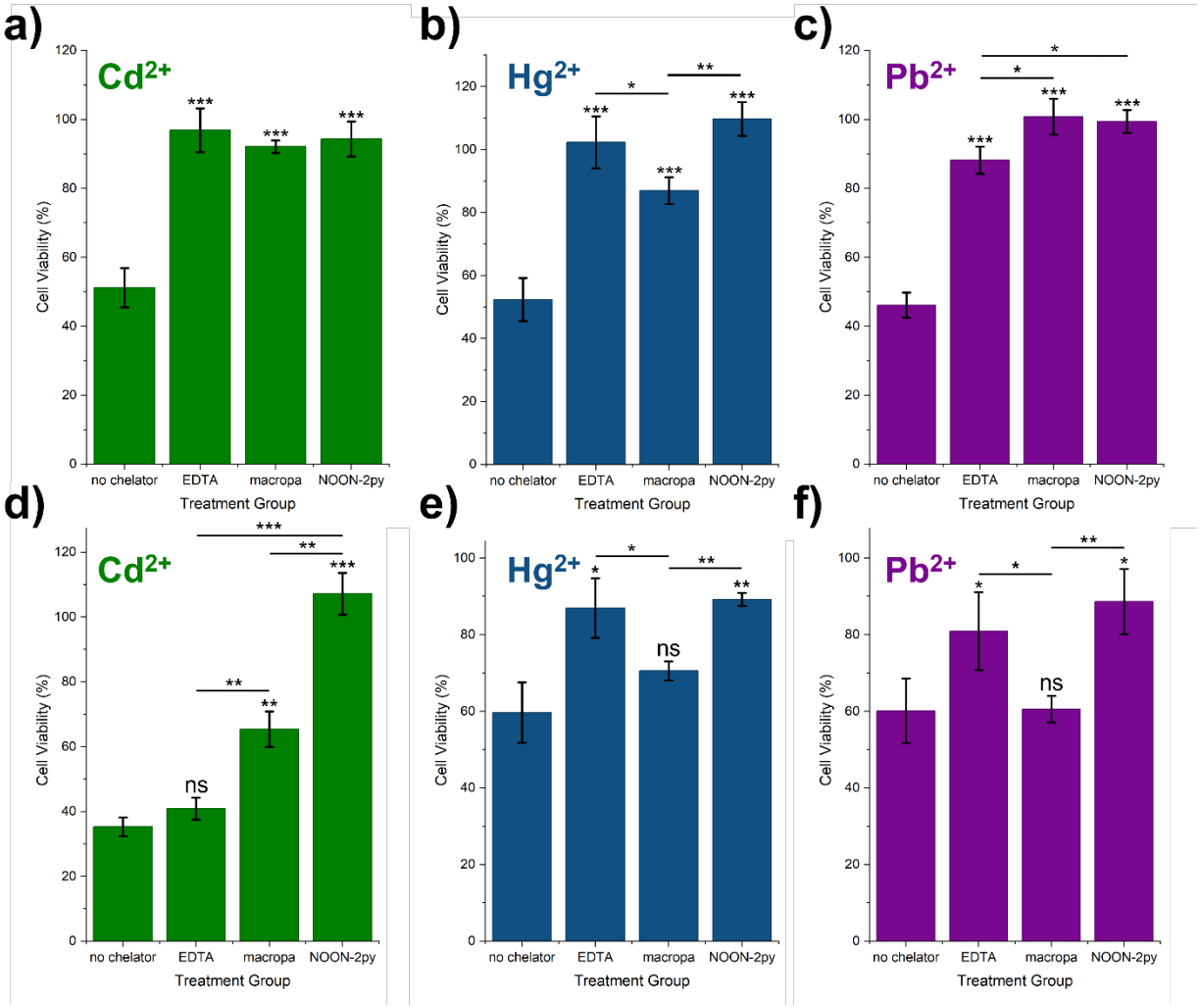

Figure 4. Cell viability of HEK293T cells treated (top) simultaneously or (bottom) with a 1-hour preincubation with Cd^{2+}, Hg^{2+}, or Pb^{2+}, then with either EDTA, macropa, or NOON-2py to evaluate chelator protective effects through cell viability (%). Top: Cell viability of HEK293T cells treated simultaneously with (a) Cd^{2+} (green), (b) Hg^{2+} (blue), or (c) Pb^{2+} (purple) and chelator. Bottom: Cell viability of HEK293T cells treated with (d) Cd^{2+} (green), (e) Hg^{2+} (blue), or (f) Pb^{2+} (purple) one hour prior to treatment with chelators. Statistical analysis was performed using the Welch's t-test, where denotations are as follows: * $p < 0.05$, ** $p < 0.01$, *** $p < 0.001$, ns = no statistical significance.

We next investigated the ability of these chelators to protect against the cytotoxic effects of Cd^{2+}, Hg^{2+}, and Pb^{2+} in HEK293T cells. Their cytoprotective effects were assessed via two distinct protocols. In the first protocol, cells were treated with the metal salt at a concentration of 0.2 µM, then immediately with the chelator at a concentration of 1 µM, and then incubated for 48 h prior to assessing their viability with the MTT dye (**Figures 4a–c**). In the absence of chelator, the metal

ion-treated cells exhibited a reduction of cell viability by approximately 50%. In the presence of the chelators, however, significant recoveries of the cell viability were observed. Of note, macropa was less effective for protecting cells from Hg^{2+} compared to NOON-2py and EDTA. This result is consistent with the lower stability constant and weaker binding of Hg^{2+} by macropa, compared to these other chelators (**Figure 4b**). Additionally, both NOON-2py and macropa were more protective against Pb^{2+} compared to EDTA (**Figure 4c**). Importantly, NOON-2py exhibited broad efficacy in ameliorating the toxic effects of all three metal ions, Cd^{2+}, Hg^{2+}, and Pb^{2+}, consistent with the large stability constants of these complexes.

For the second protocol, cells were pretreated with 0.2 μM of the metal ion for 1 h, prior to administering 1 μM of the chelator (**Figures 4d–f**). Under these conditions, the chelator would need to remove, immobilize, or detoxify intracellular metal ions, as opposed to the first protocol, where the chelators could act by sequestering the extracellular metal ions. For cells treated with Cd^{2+} under these conditions, NOON-2py and macropa were able to improve cell viability. The effects of NOON-2py, which retained the cells at close to 100% viability, however, were more significant than the minor effects of macropa. EDTA exhibited no protective effects. The improved activity of NOON-2py, compared to macropa, is consistent with its higher affinity for Cd^{2+}, whereas the inability of EDTA to protect cells may be a consequence of its impermeability to the membrane. For Hg^{2+}-treated cells, both EDTA and NOON-2py were able to protect cells in a statistically significant manner. Macropa, by contrast, was ineffective. This result reflects the poor affinity of macropa for Hg^{2+}. The ability of EDTA to protect cells under these conditions, however, is unexpected given its cell impermeability. Lastly, for cells preincubated with Pb^{2+}, those treated with NOON-2py and EDTA had significantly improved cell viability compared to those treated with macropa (**Figure 4e**). This result is unexpected when only considering relative stability constants for Pb^{2+}, indicating that other factors must be at play in the biological setting. Collectively, these results show that NOON-2py is uniformly able to protect cells against all three toxic metal ions Cd^{2+}, Hg^{2+}, and Pb^{2+}. Furthermore, because NOON-2py is effective in pretreated cells, these data also suggest that this chelator is cell-permeable.

To assess if treatment with chelators alters the cell uptake or efflux of metal ions, this property was investigated with inductively coupled plasma optical emission spectroscopy (ICP-OES). For this assay, cells were treated with 20 or 50 μM of Cd^{2+} or Pb^{2+}, and then incubated with 100 μM of the chelator. The protein content of the cells was then determined with the bicinchoninic acid (BCA) assay, and the metal content was measured by ICP-OES. For this assay, intracellular concentrations of Cd^{2+} and Pb^{2+} were amenable to detection by ICP-OES (**Figures S75–S77**). The ability of NOON-2py to sequester Cd^{2+} and Pb^{2+} in vitro was evaluated in comparison to macropa and EDTA. As shown in **Figure S75**, only NOON-2py treatment led to a statistically significant ($p < 0.01$) decrease of Cd^{2+} in the cell lysates, as reflected by a 22% lower concentration of this metal relative to the control. By contrast, none of these chelators were able to diminish intracellular Pb^{2+}. In relation to the cytotoxicity data, where NOON-2py was shown to be protective, these results

indicate that this chelator elicits this effect via intracellular sequestration of the metal ions, rather than active efflux.

2.7. Fluorescence microscopy

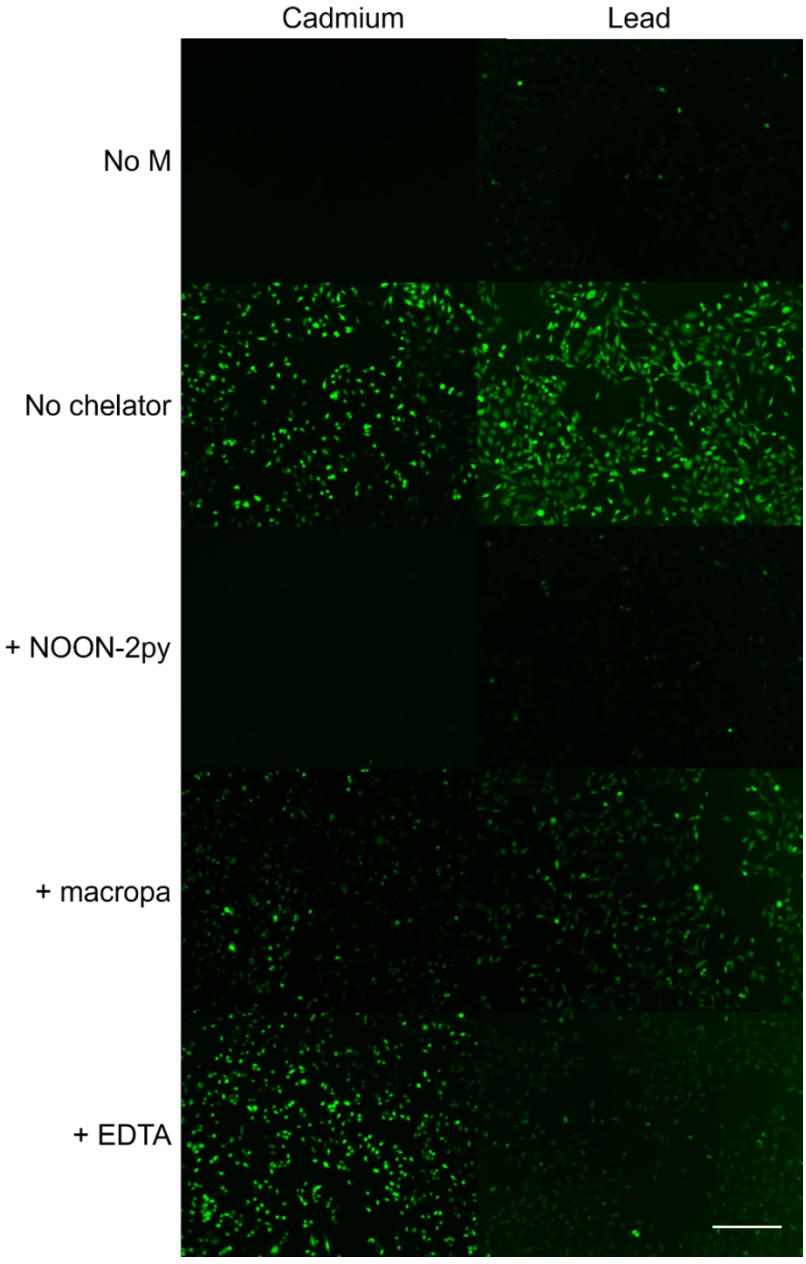

Figure 5. Fluorescence microscopy images of HeLa cells dosed with either control media + 25 μM sodium pyrithione (No M), 50 μM of M^{2+} + 25 μM sodium pyrithione in media (No chelator), or 50 μM of M^{2+} + 25 μM sodium pyrithione media, then treated with 100 μM chelator-containing media (+ chelate). Cd^{2+} treatment groups are shown on the left. Pb^{2+} treatment groups are shown on the right. Cells were stained with Leadmium Green (1 μg/mL), MitoTracker Red (0.5 μg/mL), and Hoechst dye (5 μg/mL). Scale bar indicates 300 μm.

To further evaluate the effect of chelators on intracellular metal levels, fluorescence microscopy studies were performed using the Cd^{2+}- and Pb^{2+}-selective fluorescent sensor Leadmium Green (ThermoFisher). This commercially available probe has previously been leveraged to detect labile Cd^{2+} and Pb^{2+} in live cells.[78–80] For these microscopy studies, HeLa cells were used in place of HEK293T because of their better adherence to the glass microscopy slides. The HeLa cells were incubated in media containing Hoechst dye, MitoTracker Red, and Leadmium Green before being washed and given either Cd^{2+}- or Pb^{2+}-containing media (**Figures S78–S79**) supplemented with the ionophore sodium pyrithione.[80–82] The cells were then washed, incubated with media in the absence or presence of the different chelators for 5 min, and then imaged by widefield fluorescence microscopy. As shown in **Figure 5**, both Cd^{2+}- and Pb^{2+}-treated cells exposed to NOON-2py exhibit significantly less green fluorescence than those of the cells in the absence of a chelator. Evaluation by this method showed qualitatively that NOON-2py was able to sequester intracellular Pb^{2+} and Cd^{2+} by the near total decrease in Leadmium green fluorescence intensity. Macropa and EDTA were also evaluated and still showed green fluorescence after dosage. To quantify these changes more accurately, pixel intensity was measured using *ImageJ* and the corrected total cellular fluorescence (CTCF) was determined for the green channel. As shown in **Figures S80–S81**, the NOON-2py pixel intensity matches that of the metal-free control samples for both the Cd^{2+} and Pb^{2+} treated cells, indicating complete intracellular sequestration of these metal ions.

In the Cd^{2+}-treated group, fluorescence intensity levels within cells treated with macropa were significantly lower than those not treated with a chelator. However, EDTA displayed no statistically significant difference from the positive control fluorescence intensity, indicating it has little to no interaction with Cd^{2+} inside the cell. This result is consistent with the lack of cell permeability of EDTA due to its anionic charge at physiological pH. In the Pb^{2+}-treated groups, both EDTA and macropa were only able to partially diminish the fluorescence intensity of this probe, demonstrating that under these conditions, they can still sequester Pb^{2+}, but less effectively than NOON-2py. Overall, these studies show that NOON-2py chelates both intracellular Pb^{2+} and Cd^{2+} with greater efficacy than macropa and the commonly prescribed EDTA.

2.8. Hydroxyapatite desorption

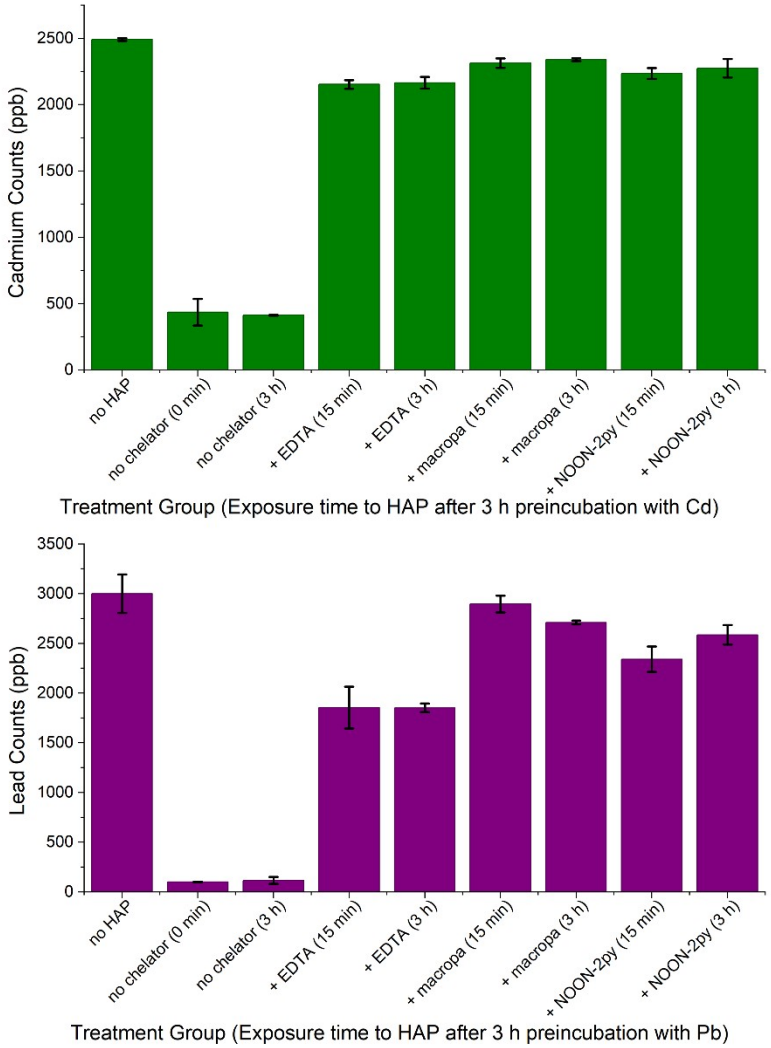

Figure 6. Hydroxyapatite desorption data for (top, green) Cd^{2+} and (bottom, purple) Pb^{2+}. Bars represent the amount of Pb^{2+} or Cd^{2+} present in HEPES buffer (pH = 7.4). The metal ions were allowed to adsorb on HAP for 3 h, prior to being treated with 40 mM of each chelator for the time point indicated.

As a final in vitro assessment of the suitability of NOON-2py for heavy metal removal, it was investigated for its ability to remove Cd^{2+} and Pb^{2+} from hydroxyapatite (HAP). HAP is the Ca^{2+} phosphate mineral that is the major inorganic component of bone.[83] During cases of Cd^{2+} and Pb^{2+} poisoning, these metal ions displace Ca^{2+} in the bone.[21,22] To determine if NOON-2py and macropa can subsequently remove Pb^{2+} and Cd^{2+} from the bone, we used an established in vitro assay (**Figure**

6).[46,84–86] Both Cd^{2+} and Pb^{2+} were adsorbed onto HAP by mixing solutions of these metal ions with solid HAP in HEPES (2-[4-(2-hydroxyethyl)piperazin-1-yl]ethanesulfonic acid) buffer. Adsorption of these metal ions was confirmed by ICP-OES (**Figure S82**), which revealed that nearly none of the metal ions remained in solution after mixing for 3 h. Once these metal ions were fully adsorbed, the HAP was further incubated in the absence or presence of 40 mM of the chelators for either 15 min or 3 h, after which the solution was measured for metal content by ICP-OES. For the HAP samples that were not treated with any chelator, no leaching of either Pb^{2+} or Cd^{2+} from the HAP was observed over the experiment duration. By contrast, all three chelators quantitatively removed Cd^{2+} from HAP within 15 min. For Pb^{2+}, however, EDTA was significantly less effective than both macropa and NOON-2py. Even after 3 h, EDTA could only remove 62.8% of the Pb^{2+} from the HAP, whereas macropa and NOON-2py removed 93.4 and 82.1%, respectively, after the same amount of time. The ability of all chelators to remove Cd^{2+} from HAP is most likely a consequence of the lower affinity of this metal ion for this phosphate-based material. Pb^{2+}, by contrast, adsorbs more strongly to HAP, limiting the applicability of these chelators.[87,88] Lastly, the observation that EDTA is less effective at removing Pb^{2+} from HAP compared to NOON-2py and macropa is in apparent contradiction to its larger Pb^{2+} stability constant. However, a likely contributing factor to the better efficacy of NOON-2py and macropa is their poor affinity for Ca^{2+}, which EDTA can bind well and likely outcompetes this ligand for Pb^{2+} within this assay. This same effect is not observed for Cd^{2+} because it has a relatively weaker binding affinity to HAP.[89] Thus, the selectivity of NOON-2py for toxic heavy metal ions marks an advantage for its use for their removal from bone.

3. Conclusion

In this work, we evaluated NOON-2py as a chelator for the binding and detoxification of Cd^{2+}, Hg^{2+}, and Pb^{2+}. This chelator leverages the diaza-18-crown-6 macrocycle to select for large metal ions, while also employing pendent pyridyl groups to stabilize metal ions of intermediate chemical hard-soft acid-base properties. Through X-ray crystallography, we identified the versatile coordination modes of NOON-2py. The largest ions studied, Ca^{2+} and Pb^{2+}, attain a conformation where the ions sit on top of the macrocycle, and the pendent pyridyl arms bind on the same face. For the smallest ion, Zn^{2+}, crystallography revealed two of these ions to bind NOON-2py, but on the outside of the macrocycle, conveying a size mismatch. Lastly, the Cd^{2+} and Hg^{2+} complexes attain a conformation where both ions are fully encapsulated by the macrocycle, and the pendent pyridyl arms bind at opposite faces. Notably, NMR spectroscopy verified the different conformations identified in the crystal structures. In addition, stability constant measurements reveal an apparent correlation between metal complex stability and the coordination mode of NOON-2py, as the most stable complexes were those of Cd^{2+}, Hg^{2+}, and Pb^{2+}. Additionally, we demonstrated the use of PAC spectroscopy for probing the Cd^{2+} complex of NOON-2py. PAC spectroscopic studies enabled us to individually detect nearly isoenergetic conformations of the complex, which were otherwise unresolvable by other spectroscopic techniques.

In investigating the ability of NOON-2py to protect cells from heavy metal toxicity, our in vitro studies revealed a good efficacy of this chelator, which is presumably a consequence of its poor affinity for endogenous metal ions like Ca^{2+} and Zn^{2+}. Although the cytotoxicity studies show that NOON-2py could generally protect cells from the cytotoxicity of Cd^{2+}, Hg^{2+}, and Pb^{2+}, there remains some ambiguity on its cellular mechanism of action, especially in comparison to EDTA and macropa. For example, NOON-2py was ineffective at decreasing the concentration of these metal ions in cells, but fluorescence microscopy studies using a Cd^{2+}- and Pb^{2+}-specific sensor indicated that it could decrease the availability of labile forms of these metal ions. This result suggests that NOON-2py is cell-permeable, marking a distinct advantage over the anionic chelator EDTA. Further studies are needed to assess the in vivo properties of NOON-2py, as pharmacokinetic properties like biodistribution and circulation half-life are expected to play a critical role for any downstream clinical applications of this chelator.

4. Experimental

4.1. General considerations

All reagents were obtained from commercial suppliers, including Sigma-Aldrich, VWR Chemicals, Ambeed, Beantown Chemicals, and ThermoScientific. They were used as received, without additional purification. The organic solvents used for reactions were of ACS grade or higher (Fisher Chemical). Solvents denoted as dry were obtained following storage over preactivated 3 Å molecular sieves. Deuterated solvents were used from Cambridge Isotope Laboratories. Ultrapure water with a resistivity of 18.2 MΩ·cm was obtained using an Elga Purelab Flex 2 water purification system. ESI-MS data were obtained on a Shimadzu LC-MS (LC-2060 3D coupled with LCMS-2050 model). The molecular ions are reported as mass-to-charge (*m/z*) ratios. Elemental analyses (C, H, N) of organic compounds were measured by Atlantic Microlab Inc. (Norcross, GA). The results are given in weight percentages.

4.2. Ligand and complex synthesis

The chelators macropa and NOON-2py were synthesized following previously described procedures.[40,45,50]

NOON-2py

The synthesis of NOON-2py was performed with a modified procedure based on prior literature reports.[40,50] 1,10-Diaza-18-crown-6 (504 mg, 1.92 mmol, 1 equiv.) and triethylamine (3.52 mL, 2.57 g, 25.4 mmol, 13.2 equiv.) were dissolved in EtOH (60 mL), and the solution was heated to 80 °C. Then, 2-(bromomethyl)pyridine hydrobromide (1.35 g, 5.32 mmol, 2.77 equiv.) was added portion-wise to the solution over 10 minutes. Upon addition, the reaction turned bright red. After 24 h, the resulting dark brown solution was removed from the heat and then cooled on ice for 4 hours. Colorless crystals of triethylamine were removed from the solution using vacuum filtration and

washed with cold EtOH. The filtrate was concentrated to dryness to obtain a brown oil. The brown oil was suspended in 5–10 mL of boiling hexanes. The mixture, while hot, was filtered through a Nylon 0.2 µm syringe membrane. This process was repeated on the residual oil 5 times. The resulting cloudy filtrate was cooled in a 5 °C refrigerator overnight. The hexanes was removed under reduced pressure to yield a yellow oil. The yellow oil was dissolved in water and lyophilized overnight to yield a pale white solid. The pale white solid was redissolved in hot hexanes and cooled to room temperature to afford crystals (800 mg, 93% yield). ^{1}H NMR (500 MHz, D_2O, pD = 5.5) δ 8.46 (d, *J* = 5.0 Hz, 2H), 7.84 (t, *J* = 7.2 Hz, 2H), 7.50 (d, *J* = 8.9 Hz, 2H), 7.39–7.36 (m, 2H), 3.81 (s, 4H), 3.65 (t, *J* = 5.7 Hz, 8H), 3.62 (s, 8H), 2.85 (t, *J* = 5.7 Hz, 8H). ^{13}C{^{1}H} NMR (126 MHz, D_2O, pD = 5.5) δ 157.27, 148.80, 138.62, 125.44, 123.81, 119.68, 70.16, 68.86, 60.37, 53.66, 1.42. [ESI-MS] found *m/z* 222.9 $[M+2H]^{2+}$, 445.1 $[M+H]^{+}$, 467.0 $[M+Na]^{+}$; calculated *m/z* 223.1 $[M+2H]^{2+}$, 445.2 $[M+H]^{+}$, 467.3 $[M+Na]^{+}$. Anal. Calcd for ($C_{24}H_{36}N_4O_4$): C, 64.84; H, 8.16; N, 12.60. Found: C, 65.04; H, 8.21; N, 12.49.

[Cd(NOON-2py)](NO_3)$_2$

NOON-2py (400 mg, 900 µmol, 1 equiv.) was dissolved in 0.3 mL of ultrapure water. $Cd(NO_3)_2{\cdot}4H_2O$ (277 mg, 897 µmol, 1 equiv.) was dissolved in 0.3 mL ultrapure water. The Cd^{2+}-containing solution was added dropwise to the NOON-2py solution, and the pH of the mixture was adjusted to 5.5 with 1 M HCl and 1 M NaOH. Immediately after pH adjustment, the reaction mixture was filtered and lyophilized overnight. The complex was isolated as a tan powder. The powder was dissolved in DMF, and large colorless crystals of this compound were obtained by allowing the vapor diffusion of tetrahydrofuran (THF) into this solution (462 mg, 92.1% yield). The NMR spectra of these crystals were measured in D_2O with a small amount of added MeCN as a chemical shift reference. ^{1}H NMR (500 MHz, D_2O, pD = 5.5) δ 8.75–8.70 (m, 2H), 8.12 (td, *J* = 7.7, 1.5 Hz, 2H), 7.64 (d, *J* = 7.5 Hz, 4H), 4.18 (s, 4H), 3.84 (dt, *J* = 11.7, 4.2 Hz, 4H), 3.69–3.63 (m, 4H), 3.47 (ddd, *J* = 11.9, 9.6, 3.0 Hz, 4H), 3.32 (ddd, *J* = 13.6, 9.6, 3.8 Hz, 4H), 3.25–3.19 (m, 4H), 2.98 (dt, *J* = 13.7, 3.7 Hz, 4H). ^{13}C{^{1}H} NMR (126 MHz, D_2O, pD = 5.5) δ 155.92, 155.84, 155.77, 149.99, 141.60, 125.69, 125.63, 125.58, 125.42, 125.37, 125.32, 68.57, 65.58, 57.86, 57.34, 1.47. [ESI-MS] found *m/z* 278.2 $[ML]^{2+}$; calculated *m/z* 278.5 $[ML]^{2+}$. Anal. Calcd for ($[Cd(C_{24}H_{36}N_4O_4)](NO_3)_2$): C, 42.36; H, 5.33; N, 12.34. Found: C, 42.36; H, 5.37; N, 12.25.

[Hg(NOON-2py)](NO_3)$_2$

NOON-2py (25.9 mg, 58.3 µmol, 1 equiv.) was dissolved in 0.3 mL of ultrapure water. $Hg(NO_3)_2{\cdot}H_2O$ (16.5 mg, 60.8 µmol, 1.04 equiv.) was dissolved in 0.3 mL ultrapure water. The solution of Hg^{2+} was added dropwise to the NOON-2py solution. A white solid precipitated out of the solution. The reaction mixture was immediately centrifuged, and the supernatant was isolated. The solid was washed with 1 mL H_2O and centrifuged. The supernatants were combined, filtered, and lyophilized. The complex was isolated as a yellow powder. The powder was dissolved in MeOH, and colorless crystals were afforded from this solution via the vapor diffusion of Et_2O (37

mg, 98.4% yield). The NMR spectra of these crystals were measured in D_2O with a small amount of added MeCN as a chemical shift reference. ^{1}H NMR (400 MHz, D_2O, pD = 5.5) δ 8.58 (d, *J* = 5.4 Hz, 2H), 8.32–8.19 (m, 2H), 7.80 (t, *J* = 7.7 Hz, 4H), 4.20 (s, 4H), 3.69 (d, *J* = 8.8 Hz, 4H), 3.57 (d, *J* = 9.7 Hz, 4H), 3.41 (q, *J* = 11.6 Hz, 8H), 3.12–2.92 (m, 8H). ^{13}C{^{1}H} NMR (126 MHz, D_2O, pD = 5.5) δ 155.10, 150.35, 143.03, 127.07, 126.12, 126.11, 119.68, 68.46, 65.45, 59.21, 59.19, 59.14, 55.32, 1.41. [ESI-MS] found *m/z* 323.0 $[ML]^{2+}$; calculated *m/z* 323.6 $[ML]^{2+}$. Anal. Calcd for ($[Hg(C_{24}H_{36}N_4O_4)](NO_3)_2$): C, 37.48; H, 4.72; N, 10.93. Found: C, 37.18; H, 4.59; N, 10.64.

$[Pb(NOON\text{-}2py)](NO_3)_2\cdot HBr\cdot NaNO_3$

NOON-2py (12.2 mg, 27.4 μmol, 1 equiv.) was dissolved in 0.3 mL of ultrapure water. $Pb(NO_3)_2$ (10.9 mg, 32.9 μmol, 1.2 equiv.) was dissolved in 0.3 mL ultrapure water. The solution of Pb^{2+} was added dropwise to the NOON-2py solution, and the pH of the mixture was adjusted to 5.5 with 1 M HCl and 1 M NaOH. Immediately after pH adjustment, the reaction mixture was filtered and lyophilized. The complex was isolated as a white powder (17 mg, 95.1% yield). The NMR spectra of the powder were measured in D_2O with a small amount of added MeCN as a chemical shift reference. ^{1}H NMR (500 MHz, D_2O, pD = 5.5) δ 8.49 (d, *J* = 5.3 Hz, 2H), 7.89 (td, *J* = 7.7, 1.7 Hz, 2H), 7.59 (d, *J* = 7.9 Hz, 2H), 7.42 (t, *J* = 6.5 Hz, 2H), 4.52 (s, 4H), 3.84 (t, *J* = 8.3 Hz, 4H), 3.65 (dd, *J* = 15.1, 8.6 Hz, 4H), 3.41 (s, 4H), 3.33–3.24 (m, 4H), 3.14 (d, *J* = 20.2 Hz, 8H). ^{13}C{^{1}H} NMR (126 MHz, D_2O, pD = 5.5) δ 159.95, 148.82, 140.35, 124.35, 124.08, 119.68, 69.63, 68.53, 64.87, 58.64, 1.40. [ESI-MS] found *m/z* 326.0 $[ML]^{2+}$; calculated *m/z* 326.6 $[ML]^{2+}$. Anal. Calcd for ($[Pb(C_{24}H_{36}N_4O_4)](NO_3)_2\cdot HBr\cdot NaNO_3$) C, 30.61; H, 3.96; N, 10.41. Found: C, 30.54; H, 3.89; N, 10.12.

$[Ca(NOON\text{-}2py)](NO_3)_2\cdot 4H_2O$

NOON-2py (26.3 mg, 59.2 μmol,1 equiv.) was dissolved in 0.3 mL of ultrapure water. $Ca(NO_3)_2\cdot 4H_2O$ (9.9 mg, 60.3 μmol, 1 equiv.) was dissolved in 0.3 mL ultrapure water. The solution of Ca^{2+} was added dropwise to the NOON-2py solution, and the pH of the mixture was adjusted to 5.5 with 1 M HCl and 1 M NaOH. Immediately after pH adjustment, the reaction mixture was filtered and lyophilized. The complex was isolated as a hygroscopic yellow oil. Colorless square plate crystals were afforded by slow evaporation of a DMF solution of this compound (28 mg, 97.7% yield). The NMR spectra of these crystals were measured in D_2O with a small amount of added MeCN as a chemical shift reference. ^{1}H NMR (500 MHz, D_2O, pD = 5.5) δ 8.51–8.49 (m, 2H), 7.72 (td, *J* = 7.7, 1.7 Hz, 2H), 7.28 (td, *J* = 7.5, 2.7 Hz, 4H), 4.05 (s, 4H), 3.72 (s, 8H), 3.24 (s, 8H), 3.07 (s, 8H). ^{13}C{^{1}H} NMR (126 MHz, D_2O, pD = 5.5) δ 157.57, 148.49, 138.60, 123.12, 122.99, 69.09, 67.80, 63.65, 57.13. [ESI-MS] found *m/z* 242.0 $[ML]^{2+}$, 546.0 $[ML(NO_3)]^+$; calculated *m/z* 242.1 $[ML]^{2+}$ 546.2 $[ML(NO_3)]^+$. Anal. Calcd for ($[Ca(C_{24}H_{36}N_4O_4)](NO_3)_2\cdot 4H_2O$): C, 42.35; H, 6.52; N, 12.35. Found: C, 42.72; H, 6.62; N, 12.55.

$[Zn_2(NOON\text{-}2py)(NO_3)_4]\cdot MeOH$

NOON-2py (25.9 mg, 58.3 μmol, 1 equiv.) was dissolved in 0.3 mL of ultrapure water. $Zn(NO_3)_2{\cdot}6H_2O$ (17.6 mg, 59.2 μmol, 1.02 equiv.) was dissolved in 0.3 mL ultrapure water. The solution of Zn^{2+} was added dropwise to the NOON-2py solution, and the pH of the mixture was adjusted to 5.5 with 1 M HCl and 1 M NaOH. Immediately after pH adjustment, the reaction mixture was filtered and lyophilized. The complex was isolated as a tan powder. The NMR spectra of these crystals were measured in D_2O with a small amount of added MeCN as a chemical shift reference. The resulting NMR spectra showed the presence of multiple species, as described in the Results and Discussion, which converged to a single compound upon the addition of an extra 1.2 eq of $Zn(NO_3)_2{\cdot}6H_2O$. Colorless, needle crystals were afforded through vapor diffusion of THF into a solution of the complex in MeOH (29 mg, 97.6% yield). ^{1}H NMR (500 MHz, D_2O) δ 8.74 (dd, J = 5.2, 1.4 Hz, 2H), 8.15 (td, J = 7.8, 1.6 Hz, 2H), 7.71–7.63 (m, 4H), 4.53 (s, 4H), 3.73–3.63 (m, 4H), 3.54 (t, J = 8.0 Hz, 4H), 3.40–3.28 (m, 4H), 3.31–3.23 (m, 4H), 3.15 (s, 4H), 3.10–3.01 (m, 4H). ^{13}C{^{1}H} NMR (126 MHz, D_2O) δ 156.06, 148.82, 143.45, 127.07, 125.65, 69.73, 66.20, 61.79, 57.22. [ESI-MS] found *m/z* 254.1 $[ML]^{2+}$, 348.7 $[M_2L(NO_3)_2]^{2+}$; calculated *m/z* 254.1 $[ML]^{2+}$, 348.1 $[M_2L(NO_3)_2]^{2+}$. Anal. Calcd for ($[Zn_2(C_{24}H_{36}N_4O_4)(NO_3)_4]{\cdot}$MeOH): C, 35.10; H, 4.71; N, 13.10. Found: C, 35.52; H, 4.49; N, 13.38.

4.3. NMR spectroscopy

NMR measurements were performed on either a Bruker Avance III HD 400 MHz with a room-temperature SmartProbe or a Bruker Avance NEO 500 MHz with a 5 mm CryoProbe Prodigy BBO probe with z-axis pulse field gradient (PFG). Low-temperature NMR measurements were performed on a Varian Unity Inova 500 MHz with a 5 mm Varian broadband probe. ^{1}H and ^{13}C chemical shifts (δ) are reported in parts per million (ppm) relative to tetramethylsilane at δ = 0, and were referenced using residual protic impurities in deuterated solvents (δ_H = 7.26 ppm; δ_C = 77.2 ppm for chloroform and δ_H = 2.06 ppm; δ_C = 1.47 ppm for MeCN) as internal references. ^{113}Cd and ^{207}Pb NMR were referenced using the substitution method. ^{113}Cd chemical shifts are reported relative to an external sample of 0.1 M $Cd(ClO_4)_2$ at δ = 0 ppm. ^{207}Pb chemical shifts are reported relative to $PbMe_4$ at δ = 0 ppm, verified with an external standard of 1 M $Pb(NO_3)_2$ in D_2O at δ = –2960 ppm. ^{199}Hg NMR chemical shifts are reported relative to $HgMe_2$ at 0 ppm, verified with an external standard of saturated $HgCl_2$ in D_2O set at δ = –1550 ppm.[90] ^{15}N chemical shifts are reported relative to $NH_3(l)$ at δ = 0 ppm. NOESY NMR spectroscopy was done with a 0.5 s mixing time. All experiments were done at 25 °C unless otherwise specified. The following abbreviations were used throughout: s = singlet, d = doublet, t = triplet, dd = doublet of doublets, etc., m = multiplet. Coupling constants (J) are given in Hz. NMR data were analyzed with MestReNova version 15.0.0-34764.

4.4. Stability and protonation constant measurements

UV-Vis spectra were recorded on a Shimadzu UV-1900 UV-vis spectrometer with a 1-cm quartz cuvette. The protonation constants of NOON-2py were determined by UV-Vis spectroscopic

titrations with a batch method. A set of solutions (15–20 samples) containing NOON-2py adjusted to different pH values was prepared. All samples were maintained at low pH ($1.30 \leq pH \leq 2.48$), and the pH was adjusted with standardized HCl (0.1 M). Under these conditions, pH cannot be accurately measured with the glass electrode; pH values were calculated directly from the concentration of HCl used in each sample. The ionic strength was fixed at 0.1 M with KCl. The pH-dependent spectroscopic data were analyzed with *HypSpec 2014* software.[91] The absorption band from 200–300 nm was used for analysis, and the molar extinction coefficients for all H_xL species (i = 0–3) were deduced in the fitting. Three independent titrations were performed. Temperature was maintained at 25 °C by a Quantum Northwest TC1 temperature controller.

Potentiometric titrations were carried out using a Metrohm Titrando 888 titrator equipped with a Ross Orion combination electrode (8103BN, ThermoFisher Scientific) and a Metrohm 806 exchange unit with an automatic burette (10 mL). This titration system was controlled by Tiamo (ver. 2.5) software. The titration vessel was fitted into a removable glass cell (~70 mL), and the temperature was maintained at 25 °C using a Vevor recirculating chiller. CO_2 was excluded from the vessel before and during the titrations by an argon flow, which was passed through an aqueous 30 wt % KOH solution. Carbonate-free KOH (0.1 M, VWR Chemicals BDH®) was standardized by potentiometric titration against potassium hydrogen phthalate (KHP). HCl (0.1 M, ThermoFisher Scientific) was standardized by potentiometric titration against Tris (base form). Tris and KHP were heated at 100 °C in a VWR lab oven for 1 hour to remove any residual water prior to calibration of the KOH and HCl solutions. Titration solutions were maintained at a constant ionic strength of 0.1 M with KNO_3 or KCl and were equilibrated for 15 minutes prior to the addition of titrant. The electrode was calibrated before each titration by titrating a solution of standardized 0.1012 M HNO_3 or 0.1001 M HCl with standardized KOH, and the data were analyzed using the program *Glee*97 (ver. 3.0.21) to obtain the standard electrode potential and slope factor.[92] Titrations were not performed until the standard potential error was ≤ 0.1.

Ligand stock solutions were made by dissolving the elementally pure solid ligand in ultrapure H_2O, and their exact concentrations were determined based on the end points of the potentiometric titration curves obtained during the protonation constant measurements. The concentrations determined from titration curves matched the concentrations calculated from the ligand masses using molecular weights obtained from elemental analysis results. M^{2+} stock solutions were made by dissolving the corresponding $M(NO_3)_2$ hydrate salts (99.999% purity or higher) in ultrapure water. Concentrations of metal in solutions were confirmed by manual titration with a 0.1 M solution of $CaNa_2EDTA$ using xylenol orange as the indicator. The solutions were inspected throughout the titrations for signs of the precipitation of metal hydroxides. Data points from the titration curves were excluded from analysis if any precipitate was observed. These titration data were refined with *Hyperquad2013* software to determine protonation and stability constants.[93] The data points within the pH range of 2.2–11.3 were used for analysis. Three titrations for each stability constant determined were carried out. Hydrolysis constants for all metal hydroxide species

and water hydrolysis constants were included in the models.[94–97] Between each data point, the method enabled up to 900 s for equilibration to account for complexation and protonation kinetics.

4.5. X-ray diffraction

Single-crystal X-ray crystallographic data and powder X-ray diffraction data were collected on a Rigaku XtaLAB Synergy Dualflex diffractometer equipped with a HyPix-Arc 100 detector and a Mo Kα X-ray source (λ = 0.71073 Å) for all crystals except the Ca^{2+} complex, for which a Cu Kα X-ray source (λ = 1.54184 Å) was used. The crystal was mounted on a cryoloop under NVH oil, and all data were collected at 100.00(10) K using an Oxford nitrogen gas cryostream. Data were collected using ω scans with 0.5° frame widths. Data collection, cell parameter determinations, integration of the data frames, and final cell parameter refinement were conducted using the CrysAlis^{Pro} program.[98] Absorption correction of the data was carried out using the SCAL3 ABSPACK method.[99] Structure determination was done using ShelXT with intrinsic phasing.[100] Structure solutions and refinements were performed using OLEX2 (version 1.5).[101] Disorder in the Hg^{2+} and Zn^{2+} structures was modeled with linked occupancies and using the restraints SADI, DELU, SIMU, and RIGU for the interatomic distances and ellipsoid size parameters. In the Ca^{2+} structure, the DFIX command was used on all water molecules to set the O–H interatomic distance to 0.84 Å. The calculated diffraction pattern spectrum was simulated in Mercury (version 2025.3.1) based on the single crystal X-ray diffraction data of the [Cd(NOON-2py)]$(NO_3)_2$ complex. Platon was used to evaluate the Ca^{2+} structure with NOON-2py with the ADDSYM function to probe for higher symmetry.[102] This analysis suggested that no obvious space group change was needed.

4.6. Perturbed angular correlation spectroscopy

4.6.1. Preparation of samples for ^{111m}Cd PAC spectroscopy

^{111m}Cd was produced and separated from the target as described previously,[68] leading to a solution of ca. 100 MBq ^{111m}Cd in 50 µL ultrapure water at the start of the sample preparation.

All samples were prepared by mixing 5–40 µL of the ^{111m}Cd solution with 10 µL $Cd(NO_3)_2{\cdot}4H_2O$ solution (of the appropriate concentration; 1.13 M or 0.113 M). Next, ultrapure water was added to get a total volume of 150 µL, and this solution was mixed with 150 µL 76 mM NOON-2py in ultrapure water (or 150 µL ultrapure water in the reference experiment with no chelator present). pH was adjusted with NaOH to a final value in the interval 5–9 (measured using pH paper). The samples were then frozen in liquid nitrogen. The sample with 38 mM NOON-2py and 37 mM Cd^{2+} was measured first at –196 ºC, then thawed and measured at 20 ºC.

The microcrystalline sample was prepared in the same manner up to and including the point where pH was adjusted. Next, the sample was evaporated to dryness by a flow of argon and warming to ca. 50 ºC for ca. 90 min, re-dissolved in 500 µL DMF, and filtered through a 0.22 µm nylon syringe

filter. Roughly half of the ^{111m}Cd activity was lost in the filter. Next, the [Cd(NOON-2py)]$^{2+}$ complex was precipitated out via the addition of 50 µL incremental additions of THF. Additional precipitate stopped being observed after a total volume of 750 µL THF was added; however, an additional 150 µL of THF was added at this point. The sample was centrifuged for 1 min in a small Eppendorf centrifuge, the supernatant removed, 1.5 mL of THF was added, centrifuged again for 1 min, the supernatant removed, and the sample was dried for ca. 15 min. A very small amount of white precipitate was formed and measured in the PAC instrument at room temperature.

4.6.2. PAC instruments and data analysis

An analogue PAC setup was used, equipped with six BaF_2 detectors.[103] The time resolution was 0.9 ns and the time-per-channel was 0.562 ns. All experiments were carried out with a distance of 36.0 mm from the sample center to the detector housing, except the microcrystalline sample, for which the distance was 14.6 mm (due to lower count rate).

Data analysis was carried out with the Prelude32 and Winfit programs using 400-800 data points (excluding the first 5 points due to systematic errors in these). A Lorentzian line shape was assumed to account for line broadening, given by the parameter δ, due to a static distribution of electric field gradients (EFGs). Fourier transformation of the data and fits were carried out using 400 points and a Kaiser-Bessel function with the window parameter equal to 4. Baseline correction for all 30 individual coincidence spectra for each experiment was done using channels –858 to –957 with respect to t_0, with the 30 values of t_0 determined using data recorded for Cd^{2+} in aqua regia.

4.6.3. Rotational diffusion of the [Cd(NOON-2py)]$^{2+}$ complex in solution derived from the ^{111m}Cd PAC data

The spectrum at 20 °C displays the expected exponentially decaying perturbation function, reflecting rapid Brownian tumbling (rotational diffusion).

The decay constant, λ (= 10.7(7) µs^{-1}), is related to the PAC parameters by[67]:

$$\lambda = 2.8\,\omega_0^2\,\tau_c\left(1+\frac{\eta^2}{3}\right)$$

Assuming that the PAC parameters recorded at –196 ºC represent those present at 20 ºC, and using only the major species (ω_0 = 0.240 rad/ns, and η = 0.67), the rotational correlation time, τ_c, may be calculated to be 58 ps.

Applying the Stokes-Einstein-Debye relation, the theoretical rotational correlation time for a molecule with molecular mass, MM = 573.58 g/mol, may be estimated, assuming a density of ρ = 1 g/cm^3, and that there is no hydration shell of the (uniform sphere) tumbling species:

$$\tau_c = \frac{\xi V}{kT} = \frac{\xi m}{kT\rho} = \frac{\xi MM}{kT\rho N_A}$$

Where ξ is the viscosity (= 0.001 Pa·s for water at 20 ºC), k is Boltzmann's constant, and T is the absolute temperature (=293 K), and $m = MM/N_A$, where N_A is Avogadro's number. This gives a theoretical estimate of the rotational correlation time of 235 ps, which is of the same order of magnitude as the experimentally derived 58 ps. The difference between the experimental and estimated theoretical τ_c may be due to the rather crude assumptions made above or to intramolecular dynamics, which is (of course) an integral part of the experimental value.

4.7. Computational details

DFT calculations for the optimization of the isomers of the [Cd(NOON-2py)]$^{2+}$ species were performed using the ORCA program package.[104–107] Geometry optimizations and vibrational frequency calculations were carried out using the PBE0 hybrid generalized gradient approximation functional.[108–110] Dispersion interactions were accounted for using the atom-pairwise D4 dispersion correction.[111–114] Scalar relativistic effects were included via the zeroth-order regular approximation (ZORA).[115] For all atoms but Cd, the def2-TZVPP basis set was employed in conjunction with ZORA recontracted basis sets.[116] The Coulomb fitting auxiliary basis SARC/J was used to accelerate integral evaluation.[116–118] For Cd, a segmented all-electron relativistically contracted basis set, developed by Pantazis et al. for use with ZORA, was employed.[119]

Solvent effects were modeled using the conductor-like polarizable continuum model with water as the dielectric medium (ε = 78.4 at 298K).[120,121] Geometry optimizations were followed by analytical frequency calculations to confirm that all stationary points are minima and to prevent any imaginary frequencies. All calculations were performed with tight self-consistent field (SCF) convergence criteria and a maximum of 750 MB of memory per core, using parallel execution over 12 processors. Modifications of the [Cd(NOON-2py)]$^{2+}$ coordinate system, specifically changing the δ/λ geometries around the macrocyclic ring, were done in GaussView (version 6.0.16). The quantum chemical calculations of the EFG of the optimized [Cd(NOON-2py)]$^{2+}$ isomers and crystal structure were carried out with the ADF program package[122,123] at the level of the spin-orbit zeroth-order regular approximation (SO-ZORA),[124,125,125–127] using the PBE0 functional,[110,128] the ZORA-QZ4P basis set[129–131] on Cd, O, N, and the ZORA-TZ2P basis set on C and H, and a Gaussian model for the nuclear charge distribution. The counterion was removed from the structure, so the total charge of the complex was 2+ (and the spin was 0). Possible linear dependencies in the basis set were removed with the DEPENDENCY keyword. The EFGs of the selected [Cd(NOON-

2py)]$^{2+}$ species optimized by DFT were calculated as previously described, and a nuclear quadrupole moment of 0.664(7) barns[71] was used to determine ω_0.

4.8. In vitro studies

4.8.1. Cytotoxicity assays

HEK293T cells were seeded in 96-well plates with ~2000 cells per well and incubated overnight at 37 °C in 5% CO_2 atmosphere. On the following day, the culture media, Dulbecco's modified Eagle medium (DMEM) + 10% fetal bovine serum (FBS), was removed, and cells were treated with media containing varying concentrations of the test compounds and further incubated for 48 h. The media was removed, and cells were incubated in DMEM containing 20% 5 mg/mL MTT for 4 h. Following incubation, the media was removed, and the purple formazan crystals were dissolved in 200 µL of dimethylsulfoxide (DMSO). The absorbance at 570 nm of each well was measured using an Agilent BioTek Synergy HTX plate reader. The average absorbance of control cells was set to 100% viability, and the average absorbances of treated cells were normalized to the control absorbance. Data were plotted as percent viability versus log[concentration]. The data was fit to a logistically function on OriginPro (2026 Learning Edition) to determine IC_{50} values. Data are reported as the average of five independent biological replicates ± SD.

4.8.2. Coincubation assays

HEK293T cells were seeded in 96-well plates with ~2000 cells per well and incubated overnight at 37 °C in 5% CO_2 atmosphere. On the following day, the culture media was removed, and cells were treated with media containing 0.2 µM $M(NO_3)_2{\cdot}nH_2O$ salt (M = Cd, Hg, Pb), and then either immediately or after 1 hour, treated with 1 µM chelator (NOON-2py, macropa, or EDTA) in media. The cells were then further incubated for 48 h. The media was removed, and cells were incubated in DMEM containing 20% 5 mg/mL MTT without FBS for 4 h. Following incubation, the media was removed, and the purple formazan crystals were dissolved in 200 µL of DMSO. The absorbance at 570 nm of each well was measured using an Agilent BioTek Synergy HTX plate reader. The average absorbance of control cells was set to 100% viability, and the average absorbances of treated cells were normalized to the control absorbance. Data is reported as the average of three independent biological replicates ± SD.

4.8.3. Metal removal assay – cadmium

HEK293T cells were plated on 100 mm × 20 mm petri dishes 72 hours prior to the experiment and cultured in growth media (DMEM + 10% FBS). Cells were then washed with 3 mL of phosphate buffered saline (PBS) and dosed with 10 mL growth media containing 20 µM $Cd(NO_3)_2{\cdot}4H_2O$. Control groups were dosed with 10 mL growth media containing no Cd^{2+}. Cells were incubated for 3 hours and then washed with 3 mL of PBS. Cells were then incubated with 10 mL of 100 µM of chelators (NOON-2py, macropa, EDTA, or DMSA). Control groups were dosed with 10 mL of

growth media with no chelators. Cells were then incubated for an additional 3 hours. After incubation, the cells were removed from the petri dishes using 3 mL trypsin and transferred to centrifuge tubes with 3 mL growth media. Cell pellets were isolated and washed with 3 × 1 mL PBS. Cells were then treated with 300 µL cold CHAPS lysis buffer (1% w/v) and shaken on ice for 30 minutes. The lysates were then aliquoted (3 × 10 µL) and their protein content was determined through BCA assay and referenced to a calibration curve of bovine serum albumin ranging from 0 to 2000 µg/mL. A 100 µL quantity of lysate was added to 2900 µL of 2% HNO_3 and Cd content was determined by ICP-OES (Avio220 Max, PerkinElmer).

4.8.4. Metal removal assay – lead

HEK293T cells were plated on 100 mm × 20 mm petri dishes 48 hours prior to the experiment and cultured in growth media (DMEM + 10% FBS). Cells were then washed with 3 mL of PBS and dosed with 10 mL growth media containing 50 µM $Pb(NO_3)_2$. Control groups were dosed with 10 mL growth media containing no Pb^{2+}. Cells were incubated for 24 hours and then washed with 3 mL of PBS. Cells were then incubated with 10 mL of 100 µM of chelators (NOON-2py, macropa, EDTA, or DMSA). Control groups were dosed with 10 mL of growth media with no chelators. Cells were then incubated for an additional 3 hours. After incubation, the cells were removed from the petri dishes using 3 mL trypsin and transferred to centrifuge tubes with 3 mL growth media. Cell pellets were isolated and washed with 3 × 1 mL PBS. Cells were then treated with 300 µL cold CHAPS lysis buffer (1% w/v) and shaken on ice for 30 minutes. The lysates were then aliquoted (3 × 10 µL) and their protein content was determined through BCA assay and referenced to a calibration curve of bovine serum albumin ranging from 0 to 2000 µg/mL. A 100 µL quantity of lysate was added to 2900 µL of 2% HNO_3 and Pb content was determined by ICP-OES (Avio220 Max, PerkinElmer).

4.8.5. Leadmium green fluorescence assay

HeLa cells were plated at a density of 1.0×10^5 cells/plate on 35 mm poly-D-lysine-coated glass-bottom dishes 24 hours prior to the experiment. The cells were then washed with 1 mL growth media (DMEM + 10% FBS) and incubated with Leadmium Green, AM dye (1 µg/mL) (Invitrogen, ThermoFisher Scientific), Hoechst dye (5 µg/mL), and MitoTracker Red (0.5 µg/mL) at room temperature for 30 minutes. After incubation, the cells were washed with 2 × 1 mL growth media and dosed with growth media containing 25 µM sodium pyrithione and 50 µM either $Cd(NO_3)_2{\cdot}4H_2O$ or $Pb(NO_3)_2$ for 5 minutes. Control plates were dosed with media containing only 25 µM sodium pyrithione. After 5 minutes, appreciable green fluorescence was observed. Cells were washed with 2 × 1 mL growth media and then incubated with growth media containing 100 µM of chelator (NOON-2py, macropa, EDTA, or DMSA). In the presence of the chelator, the cells were imaged using an EVOS M5000 Fluorescence Microscope (ThermoFisher Scientific) at 10x magnification. The visualized channels were imaged using a GFP (Green Fluorescence Protein) LED light/filter cube (470/22 nm Ex; 510/42 nm Em), DAPI (4',6-diamidino-2-phenylindole) LED

light/filter cube (357/44 nm Ex; 447/60 Em), and Texas RED LED light/filter cube (585/29 nm Ex; 624/40 nm Em). Results are reported as the average corrected total cellular fluorescence (CTCF) of 8 individual cells in 6 different areas of the dish. The corrected total cellular fluorescence of individual cells was calculated using the following equation: CTCF = ID – (A*FB), where ID is the integrated fluorescence density of the selected cell, A is the area, and FB is the mean fluorescence of the background reading. Images were processed in *ImageJ* (version 1.54g).

4.8.6. HAP Desorption assay

This in vitro desorption experiment was designed to demonstrate and compare the thermodynamic possibility of NOON-2py, EDTA, and macropa to desorb Cd^{2+} and Pb^{2+} from HAP to further support the experimental performance of the ligand removing Cd^{2+} and Pb^{2+} from bones.

Cadmium stock solutions were obtained by dissolving 30.9 mg of $Cd(NO_3)_2{\cdot}4H_2O$ in 50.0 mL HEPES buffer solution (pH = 7.4). Similarly, lead stock solutions were obtained by dissolving 33.5 mg $Pb(NO_3)_2$ in 50 mL HEPES buffer (pH = 7.4). The chelator stock solutions were made by dissolving the chelators (17.9 mg NOON-2py, 14.8 mg $CaNa_2EDTA$, and 28.5 mg macropa·2HCl·$2H_2O$) in 1.0 mL buffer solution. The samples labeled in **Figure 6** as "no HAP" contained 2.0 mL Pb^{2+} or Cd^{2+} stock solution and 0.1 mL buffer solution. The samples labeled "no chelator" in **Figure 6** contained 2.0 mL of Pb^{2+} or Cd^{2+} stock solution, 2 mg HAP, and 0.1 mL buffer solution. The samples "+ NOON-2py", "+ EDTA", "+ macropa" contained 2.0 mL Pb or Cd stock solution and 2 mg HAP initially. All solutions were mixed with a Lab Fish Orbital Shaker at 200 rpm for 3 hours. The samples "no chelator (0 min)" were then filtered in 5 mL syringes (BD syringes, Franklin Lakes, NJ) using a nylon 0.2 μm syringe filter and collected. To the "+ chelator" samples, after 3 hours of shaking, 0.1 mL of chelator solution was added to the Cd-HAP or Pb-HAP solutions. The "+ chelator (15 min)" samples were shaken for 15 minutes, and then the HAP was filtered off via syringe filter as previously noted and collected. The "+ chelator (3 h)" solutions were shaken for 3 hours before filtration. The Cd and Pb contents were determined by ICP-OES (Avio220 Max, PerkinElmer).

Mercury stock solutions were also made using 34.9 mg $Hg(NO_3)_2{\cdot}H_2O$ in 50 mL HEPES buffer (pH = 7.39). However, mercury showed no adherence to the HAP over 6 hours, consistent with its known inability to bind to bone. Thus, chelator-containing studies were not pursued with mercury.

5. Author contributions

This manuscript was written through the contributions of all authors. All of the authors have given approval to the final version of the manuscript.

6. Conflicts of interests

The authors declare no conflict of interest.

7. Data availability

All data supporting this study have been included within the article and its supplementary information (SI). CCDC 2557960-2557964 contains the supplementary crystallographic data for this paper.

8. Acknowledgments

Dr. Grant J. Stec is thanked for his assistance with the DFT analysis and experimental design. Dr. Hongjun Zhou is thanked for his assistance with all NMR experiments and Dr. Guang Wu is thanked for his assistance with all X-ray diffraction experiments. We also acknowledge Professor T. Butz for providing the Prelude32 and Winfit programs. J.R.L would like to thank the Cornell Department of Chemistry and Chemical Biology for funding under the Cornell Fellowship through the College of Arts and Sciences and the University of California, Santa Barbara for funding under the John H. Tokuyama Memorial Fellowship Endowment. The table of contents graphic was partially created in BioRender.

9. References

(1) Oldereid, N. B.; Thomassen, Y.; Attramadal, A.; Olaisen, B.; Purvis, K. Concentrations of Lead, Cadmium and Zinc in the Tissues of Reproductive Organs of Men. *J. Reprod. Fertil.* **1993**, *99*, 421–425. https://doi.org/10.1530/jrf.0.0990421.

(2) Hou, D.; Jia, X.; Wang, L.; McGrath, S. P.; Zhu, Y.-G.; Hu, Q.; Zhao, F.-J.; Bank, M. S.; O'Connor, D.; Nriagu, J. Global Soil Pollution by Toxic Metals Threatens Agriculture and Human Health. *Science* **2025**, *388*, 316–321. https://doi.org/10.1126/science.adr5214.

(3) Balali-Mood, M.; Naseri, K.; Tahergorabi, Z.; Khazdair, M. R.; Sadeghi, M. Toxic Mechanisms of Five Heavy Metals: Mercury, Lead, Chromium, Cadmium, and Arsenic. *Front. Pharmacol.* **2021**, *12*, 643972. https://doi.org/10.3389/fphar.2021.643972.

(4) Villa, J. E. L.; Peixoto, R. R. A.; Cadore, S. Cadmium and Lead in Chocolates Commercialized in Brazil. *J. Agric. Food Chem.* **2014**, *62* (34), 8759–8763. https://doi.org/10.1021/jf5026604.

(5) Nishijo, M.; Nakagawa, H.; Suwazono, Y.; Nogawa, K.; Kido, T. Causes of Death in Patients with Itai-Itai Disease Suffering from Severe Chronic Cadmium Poisoning: A Nested Case–Control Analysis of a Follow-up Study in Japan. *BMJ Open* **2017**, *7* (7), e015694. https://doi.org/10.1136/bmjopen-2016-015694.

(6) Karen Fedlscher. Lead, Mercury Levels Higher in Firefighters Who Fought L.A. Urban Blazes | Harvard T.H. Chan School of Public Health. *Harvard T.H. Chan School of Public Health*. Harvard April 3, 2025.

(7) Charkiewicz, A. E.; Omeljaniuk, W. J.; Nowak, K.; Garley, M.; Nikliński, J. Cadmium Toxicity and Health Effects—A Brief Summary. *Molecules* **2023**, *28* (18), 6620. https://doi.org/10.3390/molecules28186620.

(8) Nicholas Rees; Richard Fuller. *The Toxic Truth*; UNICEF and Pure Earth, 2020.

(9) Lee, W.-K.; Bork, U.; Gholamrezaei, F.; Thévenod, F. Cd^{2+}-Induced Cytochrome *c* Release in Apoptotic Proximal Tubule Cells: Role of Mitochondrial Permeability Transition Pore and Ca^{2+} Uniporter. *Am. J. Physiol. Renal Physiol.* **2005**, *288* (1), F27–F39. https://doi.org/10.1152/ajprenal.00224.2004.

(10) Yang, X.; Wang, B.; Zeng, H.; Cai, C.; Hu, Q.; Cai, S.; Xu, L.; Meng, X.; Zou, F. Role of the Mitochondrial Ca^{2+} Uniporter in Pb^{2+}-Induced Oxidative Stress in Human Neuroblastoma Cells. *Brain Res.* **2014**, *1575*, 12–21. https://doi.org/10.1016/j.brainres.2014.05.032.

(11) Romanova, N.; Sule, K.; Issler, T.; Hebrok, D.; Persicke, M.; Thévenod, F.; Prenner, E. J.; Lee, W.-K. Cadmium-Cardiolipin Disruption of Respirasome Assembly and Redox Balance through Mitochondrial Membrane Rigidification. *J. Lipid Res.* **2025**, *66* (3), 100750. https://doi.org/10.1016/j.jlr.2025.100750.

(12) Yuan, Y.; Zhang, Y.; Zhao, S.; Chen, J.; Yang, J.; Wang, T.; Zou, H.; Wang, Y.; Gu, J.; Liu, X.; Bian, J.; Liu, Z. Cadmium-Induced Apoptosis in Neuronal Cells Is Mediated by Fas/FasL-Mediated Mitochondrial Apoptotic Signaling Pathway. *Sci. Rep.* **2018**, *8* (1), 8837. https://doi.org/10.1038/s41598-018-27106-9.

(13) Yi, L.; Shang, X.-J.; Lv, L.; Wang, Y.; Zhang, J.; Quan, C.; Shi, Y.; Liu, Y.; Zhang, L. Cadmium-Induced Apoptosis of Leydig Cells Is Mediated by Excessive Mitochondrial Fission and Inhibition of Mitophagy. *Cell Death Dis.* **2022**, *13* (11), 928. https://doi.org/10.1038/s41419-022-05364-w.

(14) Branca, J. J. V.; Pacini, A.; Gulisano, M.; Taddei, N.; Fiorillo, C.; Becatti, M. Cadmium-Induced Cytotoxicity: Effects on Mitochondrial Electron Transport Chain. *Front. Cell Dev. Biol.* **2020**, *8*, 604377. https://doi.org/10.3389/fcell.2020.604377.
(15) Sato, M.; Takizawa, Y. Cadmium-Binding Proteins in Human Organs. *Toxicol. Lett.* **1982**, *11* (3–4), 269–273. https://doi.org/10.1016/0378-4274(82)90160-6.
(16) Ajsuvakova, O. P.; Tinkov, A. A.; Aschner, M.; Rocha, J. B. T.; Michalke, B.; Skalnaya, M. G.; Skalny, A. V.; Butnariu, M.; Dadar, M.; Sarac, I.; Aaseth, J.; Bjørklund, G. Sulfhydryl Groups as Targets of Mercury Toxicity. *Coord. Chem. Rev.* **2020**, *417*, 213343. https://doi.org/10.1016/j.ccr.2020.213343.
(17) Kägi, J. H. R.; Hapke, H.-J. Biochemical Interactions of Mercury, Cadmium, and Lead. In *Changing Metal Cycles and Human Health*; Nriagu, J. O., Ed.; Springer: Berlin, Heidelberg, 1984; pp 237–250. https://doi.org/10.1007/978-3-642-69314-4_13.
(18) Pearson, R. G. Hard and Soft Acids and Bases, HSAB, Part I: Fundamental Principles. *J. Chem. Educ.* **1968**, *45* (9), 581. https://doi.org/10.1021/ed045p581.
(19) Pearson, R. G. Hard and Soft Acids and Bases, HSAB, Part II: Underlying Theories. *J. Chem. Educ.* **1968**, *45* (10), 643. https://doi.org/10.1021/ed045p643.
(20) Johri, N.; Jacquillet, G.; Unwin, R. Heavy Metal Poisoning: The Effects of Cadmium on the Kidney. *Biometals* **2010**, *23* (5), 783–792. https://doi.org/10.1007/s10534-010-9328-y.
(21) Meltzer, L.; Kitchell, J.; Palmon, F. The Long Term Use, Side Effects, and Toxicity of Disodium Ethylenediamine Tetraacetic Acid (EDTA). *Am. J. Med. Sci.* **1961**, *242* (1), 11–17.
(22) Goering, P. L.; Waalkes, M. P.; Klaassen, C. D. Toxicology of Cadmium. In *Toxicology of Metals: Biochemical Aspects*; Goyer, R. A., Cherian, M. G., Eds.; Springer: Berlin, Heidelberg, 1995; pp 189–214. https://doi.org/10.1007/978-3-642-79162-8_9.
(23) Hamilton, J. D.; O'Flaherty, E. J. Influence of Lead on Mineralization during Bone Growth. *Fundam. Appl. Toxicol.* **1995**, *26* (2), 265–271. https://doi.org/10.1006/faat.1995.1097.
(24) Gidlow, D. A. Lead Toxicity. *Occup. Med.* **2004**, *54* (2), 76–81. https://doi.org/10.1093/occmed/kqh019.
(25) Buha, A.; Matovic, V.; Antonijevic, B.; Bulat, Z.; Curcic, M.; Renieri, E. A.; Tsatsakis, A. M.; Schweitzer, A.; Wallace, D. Overview of Cadmium Thyroid Disrupting Effects and Mechanisms. *Int. J. Mol. Sci.* **2018**, *19* (5), 1501. https://doi.org/10.3390/ijms19051501.
(26) Genchi, G.; Sinicropi, M. S.; Lauria, G.; Carocci, A.; Catalano, A. The Effects of Cadmium Toxicity. *Int. J. Environ. Res. Public Health* **2020**, *17* (11), 3782. https://doi.org/10.3390/ijerph17113782.
(27) Azar, J.; Yousef, M. H.; El-Fawal, H. A. N.; Abdelnaser, A. Mercury and Alzheimer's Disease: A Look at the Links and Evidence. *Metab. Brain Dis.* **2021**, *36* (3), 361–374. https://doi.org/10.1007/s11011-020-00649-5.
(28) Bernhoft, R. A. Mercury Toxicity and Treatment: A Review of the Literature. *J. Environ. Public Health* **2011**, *2012* (1), 460508. https://doi.org/10.1155/2012/460508.
(29) Kerper, L. E.; Hinkle, P. M. Cellular Uptake of Lead Is Activated by Depletion of Intracellular Calcium Stores. *J. Biol. Chem.* **1997**, *272* (13), 8346–8352. https://doi.org/10.1074/jbc.272.13.8346.

(30) Wax, P. M. Current Use of Chelation in American Health Care. *J. Med. Toxicol.* **2013**, *9* (4), 303–307. https://doi.org/10.1007/s13181-013-0347-2.
(31) George, T.; Brady, M. F. *Ethylenediaminetetraacetic Acid (EDTA)*; StatPearls Publishing: Treasure Island (FL), 2023.
(32) Sears, M. E. Chelation: Harnessing and Enhancing Heavy Metal Detoxification—A Review. *Sci. World J.* **2013**, *2013*, 219840. https://doi.org/10.1155/2013/219840.
(33) Tosato, M.; Ponte, F.; Franchi, S.; Menegazzo, I.; Gabryel-Skrodzka, M.; Zanoni, G.; Mancin, F.; Mäcke, H.; Jastrzab, R.; Asti, M.; Sicilia, E.; Di Marco, V. Unveiling the Potential of Sulfur-Rich Macrocyclic Chelators Against Cadmium Poisoning. *Inorg. Chem.* **2024**, *63* (50), 23970–23982. https://doi.org/10.1021/acs.inorgchem.4c04371.
(34) Tosato, M.; Verona, M.; Doro, R.; Tiezza, M. D.; Orian, L.; Andrighetto, A.; Pastore, P.; Marzaro, G.; Marco, V. D. Toward Novel Sulphur-Containing Derivatives of Tetraazacyclododecane: Synthesis, Acid–Base Properties, Spectroscopic Characterization, DFT Calculations, and Cadmium(II) Complex Formation in Aqueous Solution. *New J. Chem.* **2020**, *44* (20), 8337–8350. https://doi.org/10.1039/D0NJ00310G.
(35) Randhawa, P.; Stienstra, C. M. K.; Chen, S.; Gao, Y.; Schreckenbach, G.; Radchenko, V.; Ramogida, C. F. Development of Thiacrown Ligands for Encapsulation of Mercury-197m/g into Radiopharmaceuticals. *Dalton Trans.* **2024**, *53* (47), 18983–18997. https://doi.org/10.1039/D4DT02427C.
(36) Bjørklund, G.; Crisponi, G.; Nurchi, V. M.; Cappai, R.; Djordjevic, A. B.; Aaseth, J. A Review on Coordination Properties of Thiol-Containing Chelating Agents Towards Mercury, Cadmium, and Lead. *Molecules* **2019**, *24* (18), 3247. https://doi.org/10.3390/molecules24183247.
(37) Harriswangler, C.; L. McNeil, B.; Brandariz-Lendoiro, I.; Lucio-Martínez, F.; Valencia, L.; Esteban-Gómez, D.; F. Ramogida, C.; Platas-Iglesias, C. Exploring the Use of Rigid 18-Membered Macrocycles with Amide Pendant Arms for Pb(II)-Based Radiopharmaceuticals. *Inorg. Chem. Front.* **2024**, *11* (4), 1070–1086. https://doi.org/10.1039/D3QI02354K.
(38) Randhawa, P.; Kadassery, K. J.; McNeil, B. L.; MacMillan, S. N.; Wharton, L.; Yang, H.; Wilson, J. J.; Ramogida, C. F. The H_2S_xMacropa Series: Increasing the Chemical Softness of H_2Macropa with Sulfur Atoms to Chelate Radiometals $[^{213}Bi]Bi^{3+}$ and $[^{203}Pb]Pb^{2+}$ for Radiopharmaceutical Applications. *Inorg. Chem.* **2024**, *63* (44), 21177–21193. https://doi.org/10.1021/acs.inorgchem.4c03498.
(39) Tosato, M.; Randhawa, P.; Asti, M.; Hemmingsen, L. B. S.; O'Shea, C. A.; Thaveenrasingam, P.; Sauer, S. P. A.; Chen, S.; Graiff, C.; Menegazzo, I.; Baron, M.; Radchenko, V.; Ramogida, C. F.; Di Marco, V. Capturing Mercury-197m/g for Auger Electron Therapy and Cancer Theranostic with Sulfur-Containing Cyclen-Based Macrocycles. *Inorg. Chem.* **2024**, *63* (30), 14241–14255. https://doi.org/10.1021/acs.inorgchem.4c02418.
(40) McNeil, B. L.; Kadassery, K. J.; McDonagh, A. W.; Zhou, W.; Schaffer, P.; Wilson, J. J.; Ramogida, C. F. Evaluation of the Effect of Macrocyclic Ring Size on $[^{203}Pb]$Pb(II) Complex Stability in Pyridyl-Containing Chelators. *Inorg. Chem.* **2022**, *61* (25), 9638–9649. https://doi.org/10.1021/acs.inorgchem.2c01114.

(41) Randhawa, P.; Gower-Fry, K. L.; Stienstra, C. M. K.; Tosato, M.; Chen, S.; Gao, Y.; McDonagh, A. W.; Di Marco, V.; Radchenko, V.; Schreckenbach, G.; Ramogida, C. F. Selective Chelation of the Exotic Meitner-Auger Emitter Mercury-197 m/g with Sulfur-Rich Macrocyclic Ligands: Towards the Future of Theranostic Radiopharmaceuticals. *Chem. – Eur. J.* **2023**, *29* (21), e202203815. https://doi.org/10.1002/chem.202203815.

(42) Tosato, M.; Randhawa, P.; Lazzari, L.; McNeil, B. L.; Dalla Tiezza, M.; Zanoni, G.; Mancin, F.; Orian, L.; Ramogida, C. F.; Di Marco, V. Tuning the Softness of the Pendant Arms and the Polyazamacrocyclic Backbone to Chelate the ^{203}Pb/^{212}Pb Theranostic Pair. *Inorg. Chem.* **2024**, *63* (4), 1745–1758. https://doi.org/10.1021/acs.inorgchem.3c02610.

(43) Shannon, R. D.; Prewitt, C. T. Effective Ionic Radii in Oxides and Fluorides. *Acta Crystallogr.* **1968**, *B25*, 925–946.

(44) Ferreirós-Martínez, R.; Esteban-Gómez, D.; Tóth, É.; de Blas, A.; Platas-Iglesias, C.; Rodríguez-Blas, T. Macrocyclic Receptor Showing Extremely High Sr(II)/Ca(II) and Pb(II)/Ca(II) Selectivities with Potential Application in Chelation Treatment of Metal Intoxication. *Inorg. Chem.* **2011**, *50* (8), 3772–3784. https://doi.org/10.1021/ic200182e.

(45) Thiele, N. A.; Brown, V.; Kelly, J. M.; Amor-Coarasa, A.; Jermilova, U.; MacMillan, S. N.; Nikolopoulou, A.; Ponnala, S.; Ramogida, C. F.; Robertson, A. K. H.; Rodríguez-Rodríguez, C.; Schaffer, P.; Williams Jr., C.; Babich, J. W.; Radchenko, V.; Wilson, J. J. An Eighteen-Membered Macrocyclic Ligand for Actinium-225 Targeted Alpha Therapy. *Angew. Chem., Int. Ed.* **2017**, *56* (46), 14712–14717. https://doi.org/10.1002/anie.201709532.

(46) Thiele, N. A.; MacMillan, S. N.; Wilson, J. J. Rapid Dissolution of $BaSO_4$ by Macropa, an 18-Membered Macrocycle with High Affinity for Ba^{2+}. *J. Am. Chem. Soc.* **2018**, *140* (49), 17071–17078. https://doi.org/10.1021/jacs.8b08704.

(47) Roca-Sabio, A.; Mato-Iglesias, M.; Esteban-Gómez, D.; Tóth, É.; Blas, A. de; Platas-Iglesias, C.; Rodríguez-Blas, T. Macrocyclic Receptor Exhibiting Unprecedented Selectivity for Light Lanthanides. *J. Am. Chem. Soc.* **2009**, *131* (9), 3331–3341. https://doi.org/10.1021/ja808534w.

(48) Blei, M. K.; Waurick, L.; Reissig, F.; Kopka, K.; Stumpf, T.; Drobot, B.; Kretzschmar, J.; Mamat, C. Equilibrium Thermodynamics of Macropa Complexes with Selected Metal Isotopes of Radiopharmaceutical Interest. *Inorg. Chem.* **2023**, *62* (50), 20699–20709. https://doi.org/10.1021/acs.inorgchem.3c01983.

(49) Damu, K. V.; Shaikjee, M. S.; Michael, J. P.; Howard, A. S.; Hancock, R. D. Control of Metal Ion Selectivity in Ligands Containing Neutral Oxygen and Pyridyl Groups. *Inorg. Chem.* **1986**, *25* (22), 3879–3883. https://doi.org/10.1021/ic00242a010.

(50) Tsukube, H.; Minatogawa, H.; Munakata, M.; Toda, M.; Matsumoto, K. High-Pressure Functionalization of Diaza-Crown Ethers: New Synthesis of Ag^+ Ion-Specific Binders. *J. Org. Chem.* **1992**, *57* (2), 542–547. https://doi.org/10.1021/jo00028a027.

(51) Shul'pin, G. B. Diastereotopy in Transition Metal Complexes. *Russ. Chem. Rev.* **1980**, *49* (7), 645. https://doi.org/10.1070/RC1980v049n07ABEH002494.

(52) Kolehmainen, E. NMR Spectroscopy, Heteronuclei, Y-Cd. In *Encyclopedia of Spectroscopy and Spectrometry (Third Edition)*; Lindon, J. C., Tranter, G. E., Koppenaal, D. W., Eds.; Academic Press: Oxford, 2017; pp 366–374. https://doi.org/10.1016/B978-0-12-803224-4.00166-7.

(53) Mennitt, P. G.; Shatlock, M. P.; Bartuska, V. J.; Maciel, G. E. Cadmium-113 NMR Studies of Solid Cadmium(II) Complexes. *J. Phys. Chem.* **1981**, *85* (14), 2087–2091. https://doi.org/10.1021/j150614a027.

(54) Franklin, G. W.; Riley, D. P.; Neumann, W. L. Synthesis, Characterization and Solution ^{113}Cd NMR Analysis of Cd(II) 1,4,7,10,13-Pentaazacyclopentadecane Complexes. *Coord. Chem. Rev.* **1998**, *174* (1), 133–146. https://doi.org/10.1016/S0010-8545(97)00083-0.

(55) Kaupp, M.; von Schnering, H. G. Dominance of Linear 2-Coordination in Mercury Chemistry: Quasirelativistic and Nonrelativistic Ab Initio Pseudopotential Study of $(HgX_2)_2$ (X = F, Cl, Br, I, H). *Inorg. Chem.* **1994**, *33* (12), 2555–2564. https://doi.org/10.1021/ic00090a014.

(56) Appleton, T. G. NMR Spectroscopy, Heteronuclei, La-Hg. In *Encyclopedia of Spectroscopy and Spectrometry (Third Edition)*; Lindon, J. C., Tranter, G. E., Koppenaal, D. W., Eds.; Academic Press: Oxford, 2017; pp 342–345. https://doi.org/10.1016/B978-0-12-803224-4.00162-X.

(57) Peringer, P. ^{199}Hg Nuclear Magnetic Resonance Studies of the Mercury(II) Halides. *Inorg. Chim. Acta* **1980**, *39*, 67–70. https://doi.org/10.1016/S0020-1693(00)93636-3.

(58) Helm, M. L.; Helton, G. P.; VanDerveer, D. G.; Grant, G. J. Mercury-199 NMR Studies of Thiacrown and Related Macrocyclic Complexes: The Crystal Structures of [Hg(18S6)] $(PF_6)_2$ and $[Hg(9N3)_2](ClO_4)_2$. *Inorg. Chem.* **2005**, *44* (16), 5696–5705. https://doi.org/10.1021/ic050500z.

(59) Utschig, L. M.; Bryson, J. W.; O'Halloran, T. V. Mercury-199 NMR of the Metal Receptor Site in MerR and Its Protein-DNA Complex. *Science* **1995**, *268* (5209), 380–385.

(60) Natan, M. J.; Millikan, C. F.; Wright, J. G.; O'Halloran, T. V. Solid-State ^{199}Hg Nuclear Magnetic Resonance as a Probe of Coordination Number and Geometry in Hg(II) Complexes. *J. Am. Chem. Soc.* **1990**, *112* (8), 3255–3257. https://doi.org/10.1021/ja00164a080.

(61) Jessen, L. M.; Sauer, S. P. A.; Hemmingsen, L. ^{199}Hg NMR Shielding and Chemical Shifts of 2-, 3-, and 4-Coordinate Hg(II)-Thiolate Species. *Inorg. Chem.* **2024**, *63* (50), 23614–23619. https://doi.org/https://doi.org/10.1021/acs.inorgchem.4c03518.

(62) Bernatowicz, P.; Szymański, S.; Wrackmeyer, B. Cross-Correlation of Nuclear Quadrupolar Interactions as a Probe in Structure Elucidation: Liquid-Phase Nuclear Magnetic Resonance Studies on Bis(Hexamethyldisilylamido)Mercury(II). *J. Phys. Chem. A* **2001**, *105* (26), 6414–6419. https://doi.org/10.1021/jp010707n.

(63) Berry, S. M.; Bebout, D. C.; Butcher, R. J. Solid-State and Solution-State Coordination Chemistry of the Zinc Triad with the Mixed N,S Donor Ligand Bis(2-Methylpyridyl) Sulfide. *Inorg. Chem.* **2005**, *44* (1), 27–39. https://doi.org/10.1021/ic048915s.

(64) Junk, P. C.; Smith, M. K. Influence of Guests and Protonation on the Conformation of *N*,*N*′-Dipyridyl-Bis-Aza-18-Crown-6. *Inorg. Chem. Commun.* **2002**, *5* (12), 1082–1085. https://doi.org/10.1016/S1387-7003(02)00665-2.

(65) Wilson, J. J.; Birnbaum, E. R.; Batista, E. R.; Martin, R. L.; John, K. D. Synthesis and Characterization of Nitrogen-Rich Macrocyclic Ligands and an Investigation of Their Coordination Chemistry with Lanthanum(III). *Inorg. Chem.* **2015**, *54* (1), 97–109. https://doi.org/10.1021/ic501843c.

(66) Jensen, K. A. Tentative Proposals for Nomenclature of Absolute Configurations Concerned with Six-Coordinated Complexes Based on the Octahedron. *Inorg. Chem.* **1970**, *9* (1), 1–5. https://doi.org/10.1021/ic50083a001.
(67) Hemmingsen, L.; Sas, K. N.; Danielsen, E. Biological Applications of Perturbed Angular Correlations of γ-Ray Spectroscopy. *Chem. Rev.* **2004**, *104* (9), 4027–4062. https://doi.org/10.1021/cr030030v.
(68) Hemmingsen, L.; Bauer, R.; Bjerrum, M. J.; Zeppezauer, M.; Adolph, H. W.; Formicka, G.; Cedergren-Zeppezauer, E. Cd-Substituted Horse Liver Alcohol Dehydrogenase: Catalytic Site Metal Coordination Geometry and Protein Conformation. *Biochemistry* **1995**, *34* (21), 7145–7153. https://doi.org/10.1021/bi00021a028.
(69) Matzapetakis, M.; Farrer, B. T.; Weng, T.-C.; Hemmingsen, L.; Penner-Hahn, J. E.; Pecoraro, V. L. Comparison of the Binding of Cadmium(II), Mercury(II), and Arsenic(III) to the de Novo Designed Peptides TRI L12C and TRI L16C. *J. Am. Chem. Soc.* **2002**, *124* (27), 8042–8054. https://doi.org/10.1021/ja017520u.
(70) Iranzo, O.; Jakusch, T.; Lee, K.-H.; Hemmingsen, L.; Pecoraro, V. L. The Correlation of ^{113}Cd NMR and ^{111m}Cd PAC Spectroscopies Provides a Powerful Approach for the Characterization of the Structure of Cd^{II}-Substituted Zn^{II} Proteins. *Chemistry* **2009**, *15* (15), 3761–3772. https://doi.org/10.1002/chem.200802105.
(71) Haas, H.; Röder, J.; Correia, J. G.; Schell, J.; Fenta, A. S.; Vianden, R.; Larsen, E. M. H.; Aggelund, P. A.; Fromsejer, R.; Hemmingsen, L. B. S.; Sauer, S. P. A.; Lupascu, D. C.; Amaral, V. S. Free Molecule Studies by Perturbed γ-γ Angular Correlation: A New Path to Accurate Nuclear Quadrupole Moments. *Phys. Rev. Lett.* **2021**, *126* (10), 103001. https://doi.org/10.1103/PhysRevLett.126.103001.
(72) Chakraborty, S.; Pallada, S.; Pedersen, J. T.; Jancso, A.; Correia, J. G.; Hemmingsen, L. Nanosecond Dynamics at Protein Metal Sites: An Application of Perturbed Angular Correlation (PAC) of γ-Rays Spectroscopy. *Acc. Chem. Res.* **2017**, *50* (9), 2225–2232. https://doi.org/10.1021/acs.accounts.7b00219.
(73) Arthur E. Martell; Robert M. Smith. *Critical Stability Constants*; Plenum: New York, 1974; Vol. 1.
(74) Marcus, Y.; Eliezer, I. Mercury(II) Halide Mixed Complexes in Solution. V. Comparison of Calculated and Experimental Stability Constants. *J. Phys. Chem.* **1962**, *66* (9), 1661–1663. https://doi.org/10.1021/j100815a023.
(75) Morris, D. F. C.; Anderson, D. T.; Waters, S. L.; Reed, G. L. Zinc Chloride and Zinc Bromide Complexes—IV. Stability Constants. *Electrochim. Acta* **1969**, *14* (8), 643–650. https://doi.org/10.1016/0013-4686(69)80021-6.
(76) Ciavatta, L.; Grimaldi, M. Equilibrium Constants of Mercury(II) Chloride Complexes. *J. Inorg. Nucl. Chem.* **1968**, *30* (1), 197–205. https://doi.org/10.1016/0022-1902(68)80081-8.
(77) Foreman, H. Toxic Side Effects of Ethylenediaminetetraacetic Acid. *J. Chron. Dis.* **1963**, *16* (4), 319–323. https://doi.org/10.1016/0021-9681(63)90081-X.
(78) Johnson, C. R.; Shrout, J. D.; Fein, J. B. Visualization and Quantification of Cd Sorption to Bacteria Using Confocal Laser Scanning Microscopy and Cd-Specific Fluorescent Probes. *Chem. Geol.* **2018**, *483*, 21–30. https://doi.org/10.1016/j.chemgeo.2018.02.020.

(79) Li, Z.; Dong, T.; Pröschel, C.; Noble, M. Chemically Diverse Toxicants Converge on Fyn and C-Cbl to Disrupt Precursor Cell Function. *PLoS Biol.* **2007**, *5* (2), e35. https://doi.org/10.1371/journal.pbio.0050035.
(80) Malaiyandi, L. M.; Sharthiya, H.; Dineley, K. E. Fluorescence Detection of Intracellular Cadmium with Leadmium Green. *Biometals* **2016**, *29* (4), 625–635. https://doi.org/10.1007/s10534-016-9939-z.
(81) Lind, S. E.; Park, J. S.; Drexler, J. W. Pyrithione and 8-Hydroxyquinolines Transport Lead across Erythrocyte Membranes. *Transl. Res.* **2009**, *154* (3), 153–159. https://doi.org/10.1016/j.trsl.2009.06.002.
(82) Namdarghanbari, M. A.; Bertling, J.; Krezoski, S.; Petering, D. H. Toxic Metal Proteomics: Reaction of the Mammalian Zinc Proteome with Cd^{2+}. *J. Inorg. Biochem.* **2014**, *136*, 115–121. https://doi.org/10.1016/j.jinorgbio.2014.01.014.
(83) Wopenka, B.; Pasteris, J. D. A Mineralogical Perspective on the Apatite in Bone. *Mater. Sci. Eng. C* **2005**, *25* (2), 131–143. https://doi.org/10.1016/j.msec.2005.01.008.
(84) Wang, X.; Dai, X.; Shi, C.; Wan, J.; Silver, M. A.; Zhang, L.; Chen, L.; Yi, X.; Chen, B.; Zhang, D.; Yang, K.; Diwu, J.; Wang, J.; Xu, Y.; Zhou, R.; Chai, Z.; Wang, S. A 3,2-Hydroxypyridinone-Based Decorporation Agent That Removes Uranium from Bones In Vivo. *Nat. Commun.* **2019**, *10* (1), 2570. https://doi.org/10.1038/s41467-019-10276-z.
(85) Woods, J. J.; Unnerstall, R.; Hasson, A.; Abou, D. S.; Radchenko, V.; Thorek, D. L. J.; Wilson, J. J. Stable Chelation of the Uranyl Ion by Acyclic Hexadentate Ligands: Potential Applications for ^{230}U Targeted α-Therapy. *Inorg. Chem.* **2022**, *61* (7), 3337–3350. https://doi.org/10.1021/acs.inorgchem.1c03972.
(86) Li, W. P.; Ma, D. S.; Higginbotham, C.; Hoffman, T.; Ketring, A. R.; Cutler, C. S.; Jurisson, S. S. Development of an in Vitro Model for Assessing the in Vivo Stability of Lanthanide Chelates. *Nucl. Med. Biol.* **2001**, *28* (2), 145–154. https://doi.org/10.1016/S0969-8051(00)00196-7.
(87) Smičiklas, I.; Onjia, A.; Raičević, S.; Janaćković, Đ.; Mitrić, M. Factors Influencing the Removal of Divalent Cations by Hydroxyapatite. *J. Hazard. Mater.* **2008**, *152* (2), 876–884. https://doi.org/10.1016/j.jhazmat.2007.07.056.
(88) Smičiklas, I.; Onjia, A.; Marković, J.; Raičević, S. Comparison of Hydroxyapatite Sorption Properties towards Cadmium, Lead, Zinc and Strontium Ions. *Mater. Sci. Forum* **2005**, *494*, 405–410. https://doi.org/10.4028/www.scientific.net/MSF.494.405.
(89) Núñez, D.; Serrano, J. A.; Mancisidor, A.; Elgueta, E.; Varaprasad, K.; Oyarzún, P.; Cáceres, R.; Ide, W.; Rivas, B. L. Heavy Metal Removal from Aqueous Systems Using Hydroxyapatite Nanocrystals Derived from Clam Shells. *RSC Adv.* **2019**, *9* (40), 22883–22890. https://doi.org/10.1039/C9RA04198B.
(90) Zee, D. Z.; Singer, C. P.; O'Halloran, T. V. Chemical-Shift Standards for ^{199}Hg NMR Spectroscopy, 25 Years Later. *Inorg. Chem.* **2022**, *61* (35), 13657–13661. https://doi.org/10.1021/acs.inorgchem.2c02183.
(91) Gans, P.; Sabatini, A.; Vacca, A. Determination of Equilibrium Constants from Spectrophometric Data Obtained from Solutions of Known pH : The Program pHab. *Ann. Chim.* **1999**, *89*, 45–49.
(92) Gans, P.; O'Sullivan, B. GLEE, a New Computer Program for Glass Electrode Calibration. *Talanta* **2000**, *51* (1), 33–37. https://doi.org/10.1016/s0039-9140(99)00245-3.

(93) Gans, P.; Sabatini, A.; Vacca, A. Investigation of Equilibria in Solution. Determination of Equilibrium Constants with the HYPERQUAD Suite of Programs. *Talanta* **1996**, *43* (10), 1739–1753. https://doi.org/10.1016/0039-9140(96)01958-3.
(94) Powell, K. J.; Brown, P. L.; Byrne, R. H.; Gajda, T.; Hefter, G.; Leuz, A.-K.; Sjöberg, S.; Wanner, H. Chemical Speciation of Environmentally Significant Metals with Inorganic Ligands. Part 3: The Pb^{2+}– Cl^-, OH^-, CO_3^{2-}, SO_4^{2-}, and PO_4^{3-} Aqueous Systems. *Pure Appl. Chem.* **2009**, *81* (12), 2425–2476. https://doi.org/10.1351/PAC-REP-09-03-05.
(95) Powell, K. J.; Brown, P. L.; Byrne, R. H.; Gajda, T.; Hefter, G.; Sjöberg, S.; Wanner, H. Chemical Speciation of Environmentally Significant Heavy Metals with Inorganic Ligands. Part 1: The Hg^{2+}– Cl^-, OH^-, CO_3^{2-}, SO_4^{2-}, and PO_4^{3-} Aqueous Systems. *Pure Appl. Chem.* **2005**, *77* (4), 739–800. https://doi.org/10.1351/pac200577040739.
(96) Brown, P. L.; Ekberg, C. *Hydrolysis of Metal Ions*; John Wiley & Sons, 2016; Vol. 1.
(97) Powell, K. J.; Brown, P. L.; Byrne, R. H.; Gajda, T.; Hefter, G.; Leuz, A.-K.; Sjöberg, S.; Wanner, H. Chemical Speciation of Environmentally Significant Metals with Inorganic Ligands. Part 5: The Zn^{2+} + OH^- , Cl^- , CO_3^{2-} , SO_4^{2-} , and PO_4^{3-} Systems. *Pure Appl. Chem.* **2013**, *85* (12), 2249–2311. https://doi.org/10.1351/pac-rep-13-06-03.
(98) Agilent. CrysAlis PRO, 2014.
(99) SCALE3 ABSPACK-An Oxford Diffraction Program, 2005.
(100) Sheldrick, G. M. SHELXT – Integrated Space-Group and Crystal-Structure Determination. *Acta Crystallogr., Sect. A: Found. Adv.* **2015**, *71* (1), 3–8. https://doi.org/10.1107/S2053273314026370.
(101) Dolomanov, O. V.; Bourhis, L. J.; Gildea, R. J.; Howard, J. a. K.; Puschmann, H. *OLEX2*: A Complete Structure Solution, Refinement and Analysis Program. *J. Appl. Cryst.* **2009**, *42* (2), 339–341. https://doi.org/10.1107/S0021889808042726.
(102) Spek, A. L. Single-Crystal Structure Validation with the Program *PLATON*. *J. Appl. Crystallogr.* **2003**, *36* (1), 7–13. https://doi.org/10.1107/S0021889802022112.
(103) Butz, T.; Saibene, S.; Fraenzke, Th.; Weber, M. A "TDPAC-Camera." *Nucl. Instrum. Methods Phys. Res., Sect. A* **1989**, *284* (2), 417–421. https://doi.org/10.1016/0168-9002(89)90311-2.
(104) Frank Neese. Software Update: The ORCA Program System—Version 6.0. *WIREs: Comput. Mol. Sci.* **2025**, *15* (2), e70019. https://doi.org/10.1002/wcms.70019.
(105) Neese, F. The SHARK Integral Generation and Digestion System. *J. Comput. Chem.* **2023**, *44* (3), 381–396. https://doi.org/10.1002/jcc.26942.
(106) Neese, F. The ORCA Program System. *WIREs: Comput. Mol. Sci.* **2012**, *2* (1), 1–185. https://doi.org/10.1002/wcms.81.
(107) Neese, F.; Wennmohs, F.; Becker, U.; Riplinger, C. The ORCA Quantum Chemistry Program Package. *J. Chem. Phys.* **2020**, *152* (22), 224108. https://doi.org/10.1063/5.0004608.
(108) Neese, F.; Wennmohs, F.; Hansen, A.; Becker, U. Efficient, Approximate and Parallel Hartree–Fock and Hybrid DFT Calculations. A 'Chain-of-Spheres' Algorithm for the Hartree–Fock Exchange. *Chem. Phys.* **2009**, *356* (1–3), 98–109. https://doi.org/10.1016/j.chemphys.2008.10.036.
(109) Bykov, D.; Petrenko, T.; Izsák, R.; Kossmann, S.; Becker, U.; Valeev, E.; Neese, F. Efficient Implementation of the Analytic Second Derivatives of Hartree–Fock and Hybrid

DFT Energies: A Detailed Analysis of Different Approximations. *Mol. Phys.* **2015**, *113* (13–14), 1961–1977. https://doi.org/10.1080/00268976.2015.1025114.
(110) Carlo Adamo; Vincenzo Barone. Toward Reliable Density Functional Methods without Adjustable Parameters: The PBE0 Model. *J. Chem. Phys.* **1999**, *110* (13), 6158–6170.
(111) Caldeweyher, E.; Bannwarth, C.; Grimme, S. Extension of the D3 Dispersion Coefficient Model. *J. Chem. Phys.* **2017**, *147* (3), 034112. https://doi.org/10.1063/1.4993215.
(112) Eike Caldeweyher; Sebastian Ehlert; Andreas Hansen; Hagen Neugebauer; Sebastian Spicher; Christoph Bannwarth; Stefan Grimme. A Generally Applicable Atomic-Charge Dependent London Dispersion Correction. *J. Chem. Phys.* **2019**, *150* (15), 154122.
(113) Wittmann, L.; Gordiy, I.; Friede, M.; Helmich-Paris, B.; Grimme, S.; Hansen, A.; Bursch, M. Extension of the D3 and D4 London Dispersion Corrections to the Full Actinides Series. *Phys. Chem. Chem. Phys.* **2024**, *26* (32), 21379–21394. https://doi.org/10.1039/D4CP01514B.
(114) Grimme, S.; Antony, J.; Ehrlich, S.; Krieg, H. A Consistent and Accurate *Ab Initio* Parametrization of Density Functional Dispersion Correction (DFT-D) for the 94 Elements H-Pu. *J. Chem. Phys.* **2010**, *132* (15), 154104. https://doi.org/10.1063/1.3382344.
(115) E. van Lenthe; E. J. Baerends; J. G. Snijders. Relativistic Regular Two-component Hamiltonians. *J. Chem. Phys.* **1993**, *99* (6), 2597–4610.
(116) Weigend, F.; Ahlrichs, R. Balanced Basis Sets of Split Valence, Triple Zeta Valence and Quadruple Zeta Valence Quality for H to Rn: Design and Assessment of Accuracy. *Phys. Chem. Chem. Phys.* **2005**, *7* (18), 3297. https://doi.org/10.1039/b508541a.
(117) Neese, F. An Improvement of the Resolution of the Identity Approximation for the Formation of the Coulomb Matrix. *J. Comput. Chem.* **2003**, *24* (14), 1740–1747. https://doi.org/10.1002/jcc.10318.
(118) Weigend, F.; Häser, M.; Patzelt, H.; Ahlrichs, R. RI-MP2: Optimized Auxiliary Basis Sets and Demonstration of Efficiency. *Chem. Phys. Lett.* **1998**, *294* (1–3), 143–152. https://doi.org/10.1016/S0009-2614(98)00862-8.
(119) Rolfes, J. D.; Neese, F.; Pantazis, D. A. All-Electron Scalar Relativistic Basis Sets for the Elements Rb–Xe. *J. Comput. Chem.* **2020**, *41* (20), 1842–1849. https://doi.org/10.1002/jcc.26355.
(120) Miquel Garcia-Ratés; Frank Neese. Efficient Implementation of the Analytical Second Derivatives of Hartree–Fock and Hybrid DFT Energies within the Framework of the Conductor-like Polarizable Continuum Model. *J. Comput. Chem.* **2019**, *40* (20), 1801–1873. https://doi.org/10.1002/jcc.25833.
(121) Vincenzo Barone; Maurizio Cossi. Quantum Calculation of Molecular Energies and Energy Gradients in Solution by a Conductor Solvent Model. *J. Phys. Chem. A* **1998**, *102* (11), 1995–2001.
(122) te Velde, G.; Bickelhaupt, F. M.; Baerends, E. J.; Fonseca Guerra, C.; van Gisbergen, S. J. A.; Snijders, J. G.; Ziegler, T. Chemistry with ADF. *J. Comput. Chem.* **2001**, *22* (9), 931–967. https://doi.org/10.1002/jcc.1056.
(123) Fonseca Guerra, C.; Snijders, J. G.; te Velde, G.; Baerends, E. J. Towards an Order-N DFT Method. *Theor. Chem. Acc.* **1998**, *99* (6), 391–403. https://doi.org/10.1007/s002140050353.

(124) Chang, C.; Pelissier, M.; Durand, P. Regular Two-Component Pauli-Like Effective Hamiltonians in Dirac Theory. *Phys. Scr.* **1986**, *34* (5), 394. https://doi.org/10.1088/0031-8949/34/5/007.
(125) E. van Lenthe; R. van Leeuwen; E. J. Baerends; J. G. Snijders. Relativistic Regular Two-component Hamiltonians. *Int. J. Quantum Chem.* **1996**, *57* (3), 265–532.
(126) van Lenthe, E.; Snijders, J. G.; Baerends, E. J. The Zero-Order Regular Approximation for Relativistic Effects: The Effect of Spin–Orbit Coupling in Closed Shell Molecules. *J. Chem. Phys.* **1996**, *105* (15), 6505.
(127) E. van Lenthe; E. J. Baerends; J. G. Snijders. Relativistic Total Energy Using Regular Approximations. *J. Chem. Phys.* **1994**, *101* (11), 9783–9792.
(128) Ernzerhof, M.; Scuseria, G. E. Assessment of the Perdew–Burke–Ernzerhof Exchange-Correlation Functional. *J. Chem. Phys.* **1999**, *110* (11), 5029–5036. https://doi.org/10.1063/1.478401.
(129) Lenthe, E. V.; Baerends, E. J. Optimized Slater-type Basis Sets for the Elements 1–118. *J. Comput. Chem.* **2003**, *24* (9), 1142–1156. https://doi.org/10.1002/jcc.10255.
(130) Chong, D. P.; Van Lenthe, E.; Van Gisbergen, S.; Baerends, E. J. Even-tempered slater-type orbitals revisited: From hydrogen to krypton. *J. Comput. Chem.* **2004**, *25* (8), 1030–1036. https://doi.org/10.1002/jcc.20030.
(131) D.P. Chong. Augmenting Basis Set for Time-Dependent Density Functional Theory Calculation of Excitation Energies: Slater-Type Orbitals for Hydrogen to Krypton. *Mol. Phys.* **2005**, *103* (6–8), 749–761. https://doi.org/10.1080/00268970412331333618.